Coherent control of a $^{40}Ca^{+}$ ground state qubit

A master's thesis submitted to the faculty of mathematics, computer science and physics, of the University of Innsbruck in partial fulfillment of the requirements for the degree of

Master of Science (MSc)

carried out at the Institute of Experimental Physics under the supervision of
Dr. Philipp Schindler
o.Univ.-Prof. Dr. Rainer Blatt

presented by
Benjamin Wilhelm
June 2021

universität innsbruck

Abstract

Ion trap quantum computers use laser pulses to control the state of a qubit encoded in the ion's electronic state. In the scope of this master's thesis we present a laser beam setup to control the state of a qubit encoded in the ground state of $^{40}Ca^{+}$ ions via Raman interactions. This laser setup is used to implement single-qubit operations on one ion and two ions. We experimentally demonstrate two methods to entangle two ions with fidelities above 99 %.

Kurzfassung

Ionenfallen-Quantencomputer verwenden Laserpulse um den Zustand eines, im elektronischen Zustand des Ions kodierten, Qubits zu kontrollieren. In der vorliegenden Masterarbeit präsentieren wir einen Aufbau zur Kontrolle eines Grundzustandsqubits in $^{40}Ca^{+}$ Ionen mittels Raman-Wechselwirkungen. Dieser Aufbau wird zur Implementierung von Einzelqubitgattern an ein und zwei Ionen verwendet. Wir präsentieren zwei Methoden zur Verschränkung von zwei Ionen mit einer Güte über 99 %.

Contents

1 Introduction

The description of quantum mechanics in the early 20th century led to the development of numerous technologies that are seamlessly integrated into our daily lives. Prominent examples include semiconductor electronics, nuclear magnetic resonance technologies and laser-based communication and sensing. During the last two decades, quantum phenomena on the single-atom scale have led to the proposal and implementation of novel technologies based on the control of single particles. The emergence of these technologies has coined the term "second quantum revolution" and promises advantages over existing technologies, including secure communication, quantum computation as well as an experimental platform to gain a deeper understanding of physics.

Quantum computers are expected to outperform classical computers in certain tasks by using the laws of quantum mechanics. Algorithms performed on a quantum computer use superposition and entanglement to reduce computational complexity, therefore carrying out computations significantly faster than a classical computer. Notable examples are the Deutsch-Josza algorithm [1], Shor's algorithm for integer factorisation [2] and Grover's search algorithm [3].

A physical system capable of hosting a quantum computer needs to fulfil the requirements outlined by David DiVincenzo [4]. These are

1. A scalable physical system with well characterized qubits
2. The ability to initialize the state of the qubits to a simple fiducial state
3. Long relevant decoherence times, much longer than the gate operation time
4. A "universal" set of quantum gates
5. A qubit-specific measurement capability.

To this date, various physical implementations that fulfil these criteria have been proposed and realised, including superconducting qubits [5], photonic qubits [6], neutral atoms [7] and trapped ions. With system sizes of about 50 qubits and gate error rates on the order of 0.1 %, the currently available architectures belong to the class of "noisy intermediate-scale quantum" (NISQ) computers [8]. It has already been shown that these quantum computers are able to carry out specific algorithms faster than their classical counterparts [9]. However, for sequence lengths on the order of thousands of gates, the noise in the system is estimated to limit the performance. Fault-tolerant quantum protocols are able to mitigate this problem but will require systems with thousands of qubits. Scaling up the number of qubits without the loss of performance is currently a major challenge for all the aforementioned platforms. Trapped-ion quantum processors are a promising candidate to solve the problem of scalability by using modular architectures [10].

In a trapped-ion quantum processor, the information is stored in the electronic state of individually controllable ions. In $^{40}Ca^{+}$ ions, the most frequently used choice for a qubit is the optical qubit, encoded in the Zeeman sublevels of the $4S_{1/2}$ ground state and the metastable $3D_{5/2}$-manifold. However, precise operations on this qubit require narrow-linewidth lasers and are naturally limited by the lifetime of the $3D_{5/2}$ state. Overcoming these challenges can be done by encoding the qubit in the Zeeman states of the $4S_{1/2}$ ground state, as the lifetime of the ground state is in principle infinite.

In this work we present a setup to control a qubit encoded in the $4S_{1/2}$ ground state of trapped $^{40}Ca^{+}$ ions using Raman interactions. We use this setup to demonstrate single-qubit operations and entangling gate operations on two qubits. We aim to extend the toolbox of available operations in the ion trap experiments at Innsbruck.

This thesis is organized as follows: in chapter 2 we present a theoretical framework for the description of a single qubit as a quantum mechanical two-level system, followed by a discussion about multiple qubit systems. We then outline the working principle of a linear Paul trap and how it can be used as a quantum processor for trapped ions. Chapter 3 reviews the interaction of a laser field and a two-level ion and shows how it can be used to generate quantum operations. We expand the ion's model to a three-level system and derive how a pair of laser beams is used to obtain Raman interactions for control of a ground state qubit. This is followed by a description of two methods to generate entanglement using Raman interactions. Chapter 4 gives an overview of the ion trap setup used in this thesis. Furthermore, chapter 4 provides a description of the beam setup that is used to drive Raman interactions and was developed during the course of this thesis. In chapter 5 we present experimental results of ground state qubit control using the beam setup. We demonstrate the application of single-qubit operations, followed by the demonstration of two-qubit entanglement with different methods. Chapter 6 concludes the thesis and presents an outlook on improvements and future experiments.

2 Quantum information processing

In this chapter, we present an overview of quantum information processing with trapped ions. We start section 2.1 by introducing the quantum bit as a vector in a two-dimensional Hilbert space. In section 2.2 we present a way to visualise the qubit on a three-dimensional unit sphere and show how one can manipulate its state. We discuss entanglement of multi-qubit systems and present a figure of merit to judge the performance of entangling operations in section 2.3. Section 2.4 gives a short overview of ion dynamics in a linear Paul trap and presents an architecture for a scalable trapped ion quantum processor.

2.1 The quantum bit

In classical information theory a bit is the most fundamental unit of information and can be represented by the symbols 1 and 0. In a classical computer, a bit could, for example, be the current flowing through a transistor, where 0 and 1 correspond to no current flowing and current flowing respectively. Analogous to the classical bit, a quantum bit (qubit) [11] is the smallest unit of information in quantum information processing. It is described by two orthogonal states $|0\rangle$ and $|1\rangle$ in a two-dimensional Hilbert space. The most general pure state of a qubit $|\Psi\rangle$ is described by

$$|\Psi\rangle = \alpha\,|0\rangle + \beta\,|1\rangle\,, \tag{2.1}$$

where $\alpha, \beta \in \mathbb{C}$ are probability amplitudes and fulfil the normalisation condition $|\alpha|^2 + |\beta|^2 = 1$. The likelihood of measuring the qubit in the state $|0\rangle$ or $|1\rangle$ is given by $|\alpha|^2$ and $|\beta|^2$ respectively. If $\alpha, \beta \neq 0$, the qubit is in a superposition of $|0\rangle$ and $|1\rangle$. This is a fundamental property that distinguishes qubits from classical bits, since classical bits can only be either in the state 0 or 1. The choice of a physical system to host a qubit can be any two-level system, e.g. the polarisation of photons or electronic states of an ion. In this work our qubit is encoded the ground state manifold of the $^{40}Ca^{+}$ ion.

2.2 Bloch sphere representation and Pauli operators

Single-qubit states are commonly represented as a vector on a unit sphere, the Bloch sphere, shown in figure 2.1. Here, the south and north poles correspond to the $|1\rangle$ and $|0\rangle$ state, respectively. The qubit state $|\Psi\rangle$ can then be described with the azimuthal angle φ and the polar angle ϑ

$$|\Psi\rangle = \cos\frac{\vartheta}{2} e^{-i\frac{\varphi}{2}}\,|0\rangle + \sin\frac{\vartheta}{2} e^{i\frac{\varphi}{2}}\,|1\rangle\,. \tag{2.2}$$

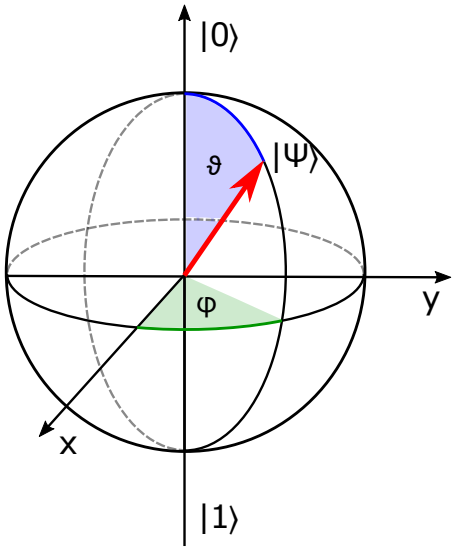

Figure 2.1: Bloch sphere for representing qubit states. The states $|0\rangle$ and $|1\rangle$ are on the north and south pole respectively. A qubit state $|\Psi\rangle$ (red arrow) is represented as a point on the surface and is fully described by the angles ϑ and φ as given in equation 2.2.

An equal superposition of qubit states is thus represented as a vector in the equatorial plane, where the angle ϕ around the z-axis describes the relative phase between the two basis states.

Similar to logic gates in classical information processing, quantum logic gates represent the building blocks of quantum information processing. A quantum logic operation is described by a unitary operator U acting on an input state $|\Psi\rangle$. For a single qubit, every quantum logic gate can be constructed from a linear combination of the Pauli operators and the identity operator $\mathbb{1}$. Writing the basis states in a vector notation, i.e. $|0\rangle = (0,1)^{\mathrm{T}}$ and $|1\rangle = (1,0)^{\mathrm{T}}$, we find the Pauli matrices in the same basis

$$\sigma_x = \begin{pmatrix} 0 & 1 \\ 1 & 0 \end{pmatrix}, \quad \sigma_y = \begin{pmatrix} 0 & -i \\ i & 0 \end{pmatrix}, \quad \sigma_z = \begin{pmatrix} 1 & 0 \\ 0 & -1 \end{pmatrix}. \tag{2.3}$$

In the Bloch sphere representation, the application of a quantum operator corresponds to a rotation around the Bloch sphere. The most general rotation by θ about a normalised vector $\boldsymbol{n} = (n_x, n_y, n_z)$ can be constructed using the Pauli operators $\boldsymbol{\sigma} = (\sigma_x, \sigma_y, \sigma_z)$ via [11]

$$R_{\mathbf{n}}(\theta) = e^{-i\frac{\theta}{2}\mathbf{n}\cdot\boldsymbol{\sigma}} = \mathbb{1}\cos\left(\frac{\theta}{2}\right) - i\sin\left(\frac{\theta}{2}\right)(n_x\sigma_x + n_y\sigma_y + n_z\sigma_z). \tag{2.4}$$

For $\boldsymbol{n} = z = (0,0,1)$ the rotation operator $R_z(\theta/2)$ describes a rotation

about the z-axis, which changes the phase φ of the qubit state. By choosing $\boldsymbol{n} = (\cos\phi, \sin\phi, 0)$ the state is rotated about a vector in the equatorial plane, yielding the rotation matrix

$$R(\theta, \phi) = \begin{pmatrix} \cos\frac{\theta}{2} & -ie^{-i\phi}\sin\frac{\theta}{2} \\ -ie^{i\phi}\sin\frac{\theta}{2} & \cos\frac{\theta}{2} \end{pmatrix}. \tag{2.5}$$

For $\phi = 0$ and $\phi = \pi/2$ we find the rotation matrices $R_x(\theta)$ and $R_y(\theta)$ that rotate the state about the x-axis and y-axis, respectively. If the state is initially in $|0\rangle$, applying $R_x(\pi/2)$ will rotate the state into an equal superposition of $|0\rangle$ and $|1\rangle$. Similarly, applying $R_x(\pi)$ to $|0\rangle$ will transfer the state from $|0\rangle$ to $|1\rangle$. The former is also called a $\pi/2$-pulse and the latter a π-pulse. In section 3.1 we present how ion-light interactions can be used for qubit rotations around the Bloch sphere.

2.3 Multiple qubits and entanglement

For a quantum processor it is required to control the state of multiple qubits. For N qubits $|\Psi\rangle_1, |\Psi\rangle_2, ..., |\Psi\rangle_N$ the total state is described by a vector of length 2^N. Multi-qubit states $|\Psi\rangle$ that are described by a product of states

$$|\Psi\rangle = |\Psi\rangle_1 \otimes |\Psi\rangle_2 \otimes ... \otimes |\Psi\rangle_N, \tag{2.6}$$

are called separable states or product states. In the presence of noise, or when the control of the system is limited, it is possible to act upon different states with different probabilities. These so-called mixed states are described by density matrices ρ [11]. For the qubit states $|\Psi_i\rangle$ with probabilities p_i, the density matrix is defined as

$$\rho = \sum_i p_i |\Psi_i\rangle \langle\Psi_i|. \tag{2.7}$$

This representation is useful when dealing with composite systems or to describe decoherence of a system.

Similar to the single-qubit gates described in section 2.2, we can define quantum gates that act on multiple qubits simultaneously. One example for a gate acting on two qubits is the controlled-NOT-gate (CNOT), which, depending on the state of a control qubit, flips the state of a target qubit. In the matrix representation it can be written as

$$U_{\text{CNOT}} = \begin{pmatrix} 1 & 0 & 0 & 0 \\ 0 & 1 & 0 & 0 \\ 0 & 0 & 0 & 1 \\ 0 & 0 & 1 & 0 \end{pmatrix}. \tag{2.8}$$

Combining the CNOT-gate and single-qubit operations, one can implement any arbitrary unitary operations. This is referred to as a universal set of quantum

gates and is a requirement for universal quantum computing as introduced by the DiVincenzo criteria.

If the multi-qubit state is not a product state of the individual qubit states, the state is entangled. Entanglement is the key property that distinguishes quantum systems from classical systems. For two qubits, the possible entangled states are described by the Bell states

$$|\Phi^{\pm}\rangle = \frac{1}{\sqrt{2}}(|00\rangle \pm e^{i\phi}|11\rangle), \tag{2.9}$$

$$|\Psi^{\pm}\rangle = \frac{1}{\sqrt{2}}(|01\rangle \pm e^{i\phi}|10\rangle), \tag{2.10}$$

where we used the notation $|ij\rangle = |i\rangle_1 \otimes |j\rangle_2$. These states are of fundamental interest for quantum communication protocols, as they can be used for secure key distribution methods that detect attempts of eavesdropping [12]. Entangled states can be created by using entangling gates, i.e. unitary operations that create an entangled state from a separable input state.

In this thesis we use different sets of quantum gates to create the Bell state $|\Phi^+\rangle$. However, due to imperfections in our gate operations, the measured state, represented by the density matrix ρ, may differ from the desired Bell state. We can quantify the similarity between ρ and $|\Phi^+\rangle$ by using the fidelity

$$F = \langle\Phi^+|\,\rho\,|\Phi^+\rangle\,. \tag{2.11}$$

The fidelity represents the probability of finding the system in the desired state. The infidelity, defined as $1 - F$, represents the deviation from the target state and is used to quantify the error rate of the entangling gate operation under the assumption that the observed error is not coming from state preparation or measurement errors. In section 5.3.3 we present an efficient way to measure the fidelity. We use this as a figure of merit to judge the performance of our entangling gate operations implemented in chapter 5.

2.4 Linear Paul Trap for a quantum processor

Ions have proven to be a viable candidate for quantum information processing, as their electronic structure offers the possibility to encode a qubit and ion-light interactions can be used to implement quantum logic gates. Since ions are charged particles, they can be trapped using Coulomb interactions. As a consequence of Maxwell's equations, it is not possible to create a confining potential in all three dimensions solely by using electrostatic fields. A common method to circumvent this restriction is using a combination of static and dynamic, time-varying electric fields. Ion traps that use this method are called Paul traps.

A schematic representation of a linear Paul trap is presented in figure 2.2. It consists of four parallel rod electrodes that create a time-varying, radio-frequency, potential in the radial xy-plane. Two additional endcap electrodes create a static confining potential in the axial z-direction. The radio-frequency potential is described by [13]

$$\Phi_{\mathrm{rf}}(\boldsymbol{r}, t) = V_{\mathrm{rf}} \frac{(x^2 - y^2)\cos(\Omega_{\mathrm{rf}} t)}{2r_0^2}, \tag{2.12}$$

where V_{rf} denotes the voltage applied to the electrodes, and Ω_{rf} the frequency of the rf-drive. The factor r_0 describes a characteristic distance from the trap center to the electrodes and also includes the shape of the trap electrodes. The radial potential creates a periodically varying confinement in one radial direction and anti-confinement in the other. Similarly, applying a static voltage U_{dc} to the endcaps creates the potential

$$\Phi_{\mathrm{dc}}(\boldsymbol{r}) = U_{\mathrm{dc}} \frac{(2z^2 - x^2 - y^2)}{z_0^2}, \tag{2.13}$$

with z_0 denoting a geometric factor that depends on the electrode shape and their separation. The static potential creates a constant axial confinement and radial anti-confinement. The total potential is the sum of the static and dynamic potential, i.e. $\Phi = \Phi_{\mathrm{rf}} + \Phi_{\mathrm{dc}}$.

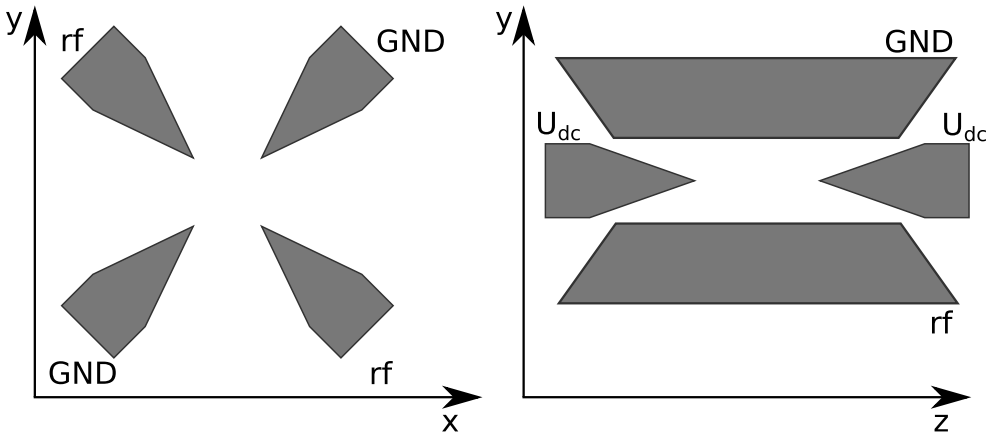

Figure 2.2: Schematic electrode layout of a three-dimensional linear Paul trap. It consists of four electrodes in the xy-plane and two electrodes along the z-axis. Confinement in the radial plane (left) is created by applying a radio-frequency voltage to two rod electrodes. In the axial direction (right), confinement is generated via electrostatic fields created by the two endcap electrodes.

The ion's motion in the trap is determined by the total potential. For an ion with charge e and mass m, the equations of motion are given by

$$m\frac{\partial^2 \boldsymbol{r}}{\partial t^2} = -e\nabla\Phi. \tag{2.14}$$

This equation takes the form of the Mathieu equations [14]. For a given m and e one can find parameters $\Omega_{\mathrm{rf}}, V_{\mathrm{rf}}, U_{\mathrm{dc}}$ that yield stable solutions of $\boldsymbol{r}$. For a stable solution of eq. 2.14 one finds that the ion's motion can be decomposed into a harmonic part, and a fast driven motion with frequency Ω_{rf}, called micromotion. In the secular approximation the micromotion can be neglected and the motion is determined by the pseudopotential Ψ, i.e. the harmonic potential

$$e\Psi = \frac{1}{2}\sum_{i=x,y,z} m\omega_i^2 r_i^2, \tag{2.15}$$

with ω_i denoting the frequency of the ion's harmonic motion. Usual trap frequencies ω_i are on the order of 1 MHz, resulting in a wave packet size of the ground state on the order of 10 nm. In trapped ion quantum computation the motional degree of freedom is used to create an entangling gate operation as will be discussed in chapter 3. In this thesis we are mainly concerned about the motion along the z-axis. The frequency of the harmonic motion along the z-axis can be found by solving equation 2.14 for the static potential and is given by

$$\omega_z = \sqrt{\frac{2eU_{\mathrm{dc}}}{mz_0^2}}. \tag{2.16}$$

In the experiment we are able to tune the motional frequency ω_z by varying U_{dc}.

When trapping two or more ions, the motion of the ions is coupled due to their Coulomb interaction. This leads to the appearance of additional motional modes in the axial and radial direction since the ions' motion is coupled through the Coulomb repulsion. In the case of two ions with equal mass, the two normal axial motional modes are the center of mass (COM) mode at frequency ω_z and the breathing mode at frequency $\sqrt{3}\omega_z$ [15].

Besides the additional motional modes, the Coulomb potential created by one ion shifts the equilibrium position of the other ion within the potential, and vice versa. In order to maximise the efficiency of the light-shift gate discussed in section 3.3.1, the equilibrium distance between the ions needs to be controlled precisely. Considering two ions with identical mass, the axial equilibrium position is symmetric around the potential minimum, with the distance between the ions [16]

$$\Delta z = \left(\frac{e^2}{2\pi\epsilon_0 m\omega_z^2}\right)^{1/3}. \tag{2.17}$$

Since $\omega_z \propto \sqrt{U_{\mathrm{dc}}}$, we can tune the endcap voltages to adjust the ion spacing Δz. In section 5.3.1 we demonstrate the effect of Δz on the coupling between the

individual motional modes and a light field. From equation 2.17 one can see that trap frequencies on the order of 1 MHz result in an inter-ion spacing of 4 µm-5 µm, whereas typical ion-light interaction wavelengths are on the order of 400-1000 nm. This allows one to individually address single ions and thus realise a universal quantum computer.

One of the largest challenges for ion trap quantum computers to date is being able to increase the number of qubits without loss of performance. Current ion trapping teams are able to operate 10-50 qubits [17]. Noisy intermediate-scale quantum technology requires 50-100 qubits to surpass the performance of classical computers and more than 1000 qubits are required to perform fault-tolerant quantum computation. Increasing the number of ions makes the ion string heavier, thus more laser power is required to manipulate the ion string. The number of motional modes increases linearly with the number of ions, which leads to interference effects that worsen the quality of qubit operations. This problem can be overcome by separating a large ion string into multiple smaller ion strings confined in separated trapping registers [10]. One way to create separate trapping registers is by segmenting the electrodes of the Paul trap.

In our experiment we use a two-dimensional surface trap architecture with segmented electrodes. A schematic layout is presented in figure 2.3. In a surface trap the confining potentials are created by a two-dimensional array of electrodes. Similar to the three-dimensional case, one uses static and dynamic potentials to create a confining pseudopotential. By using individually controllable segmented electrodes, one gains more degrees of freedom for shaping the electric potential in each register. For example, this allows shuttling the ions between registers [18], rotating the ions within one register [19] and splitting an ion crystal [20].

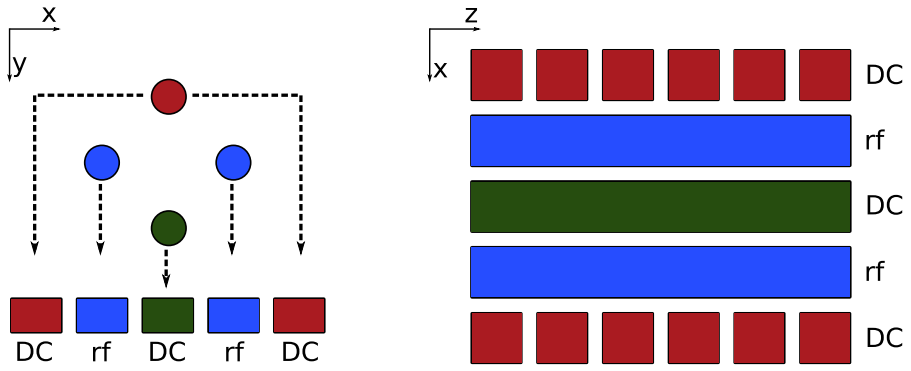

Figure 2.3: Schematic illustration of a two-dimensional surface trap. Similar to a three-dimensional trap, static (dc) and rf voltages are applied to a flat array of electrodes to create a confining pseudopotential. In a segmented surface trap electrodes are divided into individually controllable segments, which grants more degrees of freedom for shaping the electric potential.

3 Ion-Light Interactions

Coherent, electromagnetic fields can be used to control an ion's electronic as well as its motional states. In this chapter, we describe the interaction between a trapped ion and a coherent electromagnetic field, created by a laser. In section 3.1 we model the ion as a two-level system and demonstrate the effect of light on the electronic and motional states. We expand this model to a three-level system in section 3.2 and present its interaction with two laser fields in the far detuned regime. From this we derive Raman interactions that reduce the three-level system to an effective two-level system. Finally, section 3.3 describes entangling gate operations mediated by Raman interactions.

3.1 Two-level Atom

Here, we will introduce the interaction between a trapped ion and an electromagnetic field, by considering an ion that consists only of the excited state $|e\rangle$ and ground state $|g\rangle$. The states are separated by the energy $\hbar\omega$. The trapped ion's motion can be described by a harmonic oscillator with frequency ω_z. The Hamiltonian of the ion is then

$$H_0 = \frac{\hbar\omega}{2}\sigma_z + \hbar\omega_z a^\dagger a, \tag{3.1}$$

where a and $a^\dagger$ denote the annihilation and creation operators of the harmonic oscillator mode. By shining a single-mode laser onto the ion, we introduce an interaction between the laser field and the ion. The laser field at time t and a given position $\boldsymbol{r}$ is described by a monochromatic plane wave

$$\boldsymbol{E_L}(\boldsymbol{r},t) = \frac{\boldsymbol{\epsilon}E_0}{2}\left(e^{i(\boldsymbol{k_L}\cdot\boldsymbol{r}-\omega_L t+\phi_L)} + e^{-i(\boldsymbol{k_L}\cdot\boldsymbol{r}-\omega_L t+\phi_L)}\right), \tag{3.2}$$

where $\boldsymbol{\epsilon}$ denotes the polarization, E_0 the field amplitude, $\boldsymbol{k_L}$ the wavevector, ϕ_L the laser phase and ω_L the laser frequency. A schematic of the two-level ion-light interaction is shown in figure 3.1.

The coupling strength between the ion and the laser field is found by first defining the dipole operator $\boldsymbol{d} = e\boldsymbol{r}$ [21]. The Rabi frequency $\Omega = E_0 \langle e|\, \boldsymbol{d}\cdot\boldsymbol{\epsilon}\, |g\rangle / \hbar$ then describes the coupling strength between the ion and the electromagnetic field [21]. From this, one finds the Hamiltonian describing the ion-light interaction

$$H_I = -\frac{\hbar\Omega}{2}\left(\sigma_- + \sigma_+\right)\left(e^{i(k_L r-\omega_L t+\phi_L)} + e^{-i(k_L r-\omega_L t+\phi_L)}\right). \tag{3.3}$$

Here, $\sigma_- = |g\rangle\langle e|$ and $\sigma_+ = |e\rangle\langle g|$ denote the electronic lowering and raising operators.

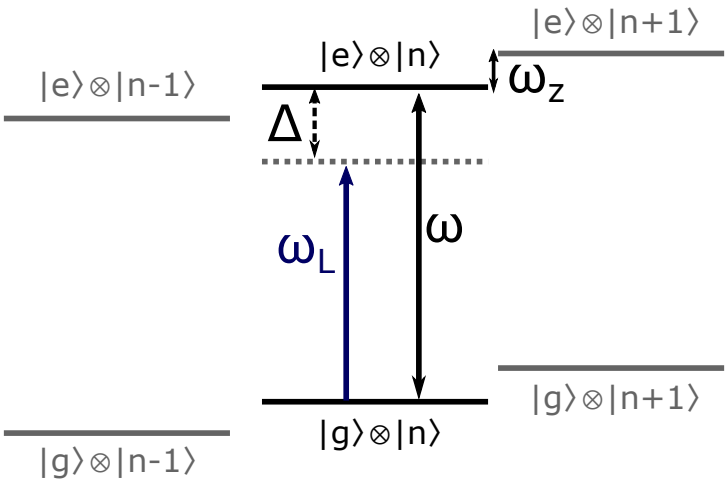

Figure 3.1: Two-level atom interacting with a laser field. The ground state $|g\rangle$ and excited state $|e\rangle$ are separated by the energy $\hbar\omega$. The laser field with frequency ω_{L} is detuned by $\Delta = \omega_{\mathrm{L}} - \omega$ from the electronic transition. The shaded lines represent the structure of the harmonic oscillator with frequency ω_z and mode occupation number n.

For analysing the dynamics of the system it is useful to transform the full Hamiltonian $H = H_0 + H_{\mathrm{I}}$ into the interaction picture by using the unitary transformation $U = \exp(iH_0t/\hbar)$, which transforms the Hamiltonian $H \to \tilde{H} = UHU^\dagger + i\hbar\dot{U}U^\dagger$. For simplicity, we neglect the ion's motion for now and continue with the electric dipole approximation $\exp(i\boldsymbol{k_{\mathrm{L}}} \cdot \boldsymbol{r}) \approx 1$, which is valid if the wavelength is much larger than the size of the ion [21]. It should be noted that the coupling to the ion's motion is important for cooling of the ion as well as the implementation of entangling gates discussed in chapter 5. Switching into the interaction picture, we find the interaction Hamiltonian

$$\begin{aligned}\tilde{H} &= UHU^\dagger + i\hbar\dot{U}U^\dagger \\ &= -\frac{\hbar\Omega}{2}\Big(\sigma_- e^{i(-(\omega_{\mathrm{L}}+\omega)t+\phi_{\mathrm{L}})} + \sigma_- e^{-i(-(\omega_{\mathrm{L}}-\omega)t+\phi_{\mathrm{L}})} \\ &\qquad + \sigma_+ e^{-i((\omega_{\mathrm{L}}-\omega)t+\phi_{\mathrm{L}})} + \sigma_+ e^{i((\omega_{\mathrm{L}}+\omega)t+\phi_{\mathrm{L}})}\Big) \\ &= -\frac{\hbar\Omega}{2}\left(\sigma_+ e^{i(-\Delta t+\phi_{\mathrm{L}})} + \sigma_- e^{-i(-\Delta t+\phi_{\mathrm{L}})}\right).\end{aligned} \tag{3.4}$$

This Hamiltonian includes one term oscillating at the frequency of the detuning $\Delta = \omega_{\mathrm{L}} - \omega_0$ and a faster oscillation with frequency $\omega_{\mathrm{L}} + \omega_0$. If $2\omega_{\mathrm{L}} \gg \sqrt{\Omega^2 + \Delta^2}$ we can use the rotating wave approximation (RWA) and neglect the fast oscillating terms [14]. Next, we describe the evolution of the states. We can write the

quantum state of the two-level atom in the interaction picture as

$$|\tilde{\psi}(t)\rangle = c_{\mathrm{e}}(t)\,|\tilde{e}\rangle + c_{\mathrm{g}}(t)\,|\tilde{g}\rangle\,, \tag{3.5}$$

where $c_{\mathrm{e}}(t)$ and $c_{\mathrm{g}}(t)$ are now time-dependent probability amplitudes. Here, $|\tilde{e}\rangle$ and $|\tilde{g}\rangle$ represent the excited state and the ground state in the interaction picture. Solving the Schrödinger equation in the interaction picture yields for the coefficients

$$\begin{pmatrix}\dot{c}_{\mathrm{e}}(t)\\ \dot{c}_{\mathrm{g}}(t)\end{pmatrix} = -\frac{i\Omega}{2}\begin{pmatrix}0 & e^{i(-\Delta t-\phi_{\mathrm{L}})}\\ e^{-i(-\Delta t-\phi_{\mathrm{L}})} & 0\end{pmatrix}\begin{pmatrix}c_{\mathrm{e}}(t)\\ c_{\mathrm{g}}(t)\end{pmatrix}. \tag{3.6}$$

Note that on resonance, i.e. $\Delta = 0$, this equation becomes time-independent. Equation 3.6 can be solved by means of a Laplace transform [14], yielding the propagator

$$U(t) = \begin{pmatrix} e^{-i\frac{\Delta t}{2}}\left(\cos\left(\frac{\Omega' t}{2}\right) + \frac{i\Delta\sin\left(\frac{\Omega' t}{2}\right)}{\Omega'}\right) & -i\frac{\Omega}{\Omega'}e^{-i(\phi_{\mathrm{L}}+\frac{\Delta t}{2})}\sin\left(\frac{\Omega' t}{2}\right)\\ -i\frac{\Omega}{\Omega'}e^{i(\phi_{\mathrm{L}}+\frac{\Delta t}{2})}\sin\left(\frac{\Omega' t}{2}\right) & e^{i\frac{\Delta t}{2}}\left(\cos\left(\frac{\Omega' t}{2}\right) - \frac{i\Delta\sin\left(\frac{\Omega' t}{2}\right)}{\Omega'}\right)\end{pmatrix}, \tag{3.7}$$

where we defined $\Omega' = \sqrt{\Delta^2 + \Omega^2}$. For a resonant laser field, i.e. $\Delta = 0$, equation 3.7 is equivalent to the rotation matrix $R(\theta, \phi)$ described in equation 2.5. Therefore, one can use resonant laser interactions to induce single-qubit rotations on the Bloch sphere to control the qubit state. We use this in section 5.2 to realise and describe single-qubit operations and implement Ramsey and spin-echo sequences.

Applying equation 3.7 to the initial state $|g\rangle$ yields the probability $p_e(t)$ to find the ion in the excited state

$$p_e(t) = |\,\langle e|\,U(t)\,|g\rangle\,|^2 = \frac{\Omega^2}{\Omega'^2}\sin^2\left(\frac{\Omega' t}{2}\right). \tag{3.8}$$

If $\Delta \neq 0$, the qubit state acquires an additional phase proportional to Δt and the trajectory on the Bloch sphere deviates from the resonant case. As can be seen in figure 3.2, this deviation grows with the magnitude of the detuning. In addition to the acquired phase, if $\Delta \neq 0$, we find $p_e(t) < 1$, making it impossible to fully transfer population from $|g\rangle$ to $|e\rangle$. Therefore, it is important to use resonant laser fields when trying to realise population transfer.

From equation 3.8 we see that the ion is periodically oscillating around the Bloch sphere as long as it is interacting with the laser. These periodic rotations are called Rabi oscillations [21] and are shown in figure 3.2 for different Δ. It can be seen that larger detunings lead to faster oscillations, but reduce the population one can observe in the state $|e\rangle$.

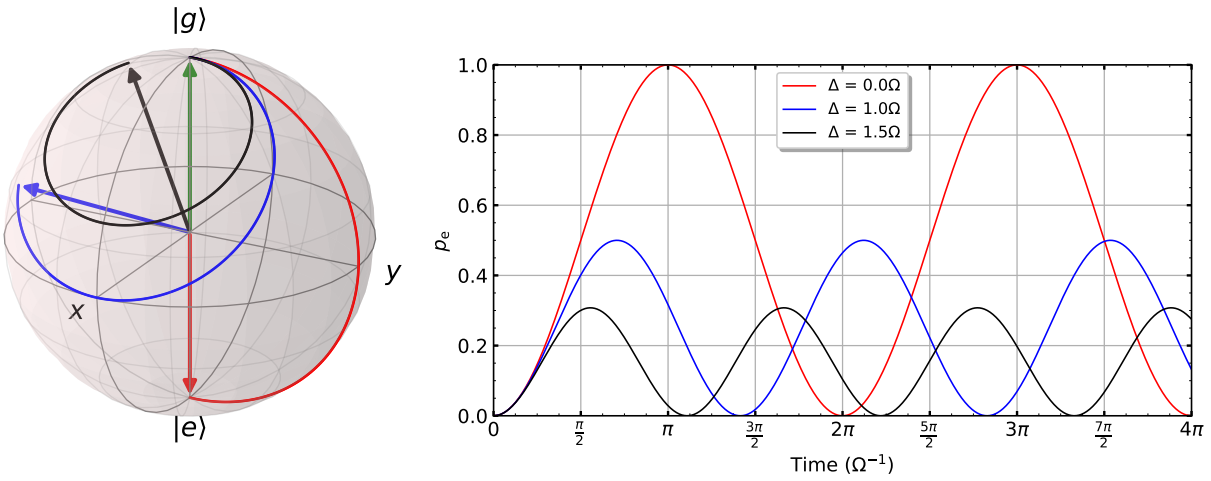

Figure 3.2: State evolution of a two level system interacting with resonant and off-resonant laser fields. Left image shows the effect of the propagator $U(t = \pi/\Omega)$ on an initial state $|g\rangle$ (green arrow) for different Δ. Red, blue and black arrows indicate the state after evolution time π/Ω. Right image shows Rabi oscillations given in equation 3.8. Note that p_e represents the projection of the state vector onto the z-axis.

Ramsey and spin-echo sequences

In an experiment we are able to control the laser parameters Ω, Δ, ϕ_{L} and the time t it interacts with the ion. We can therefore tailor the propagator $U(t, \Omega, \Delta, \phi_{\mathrm{L}})$ from equation 3.7, allowing us to control the ion's state on the Bloch sphere. With control over the ion's state, we are able to perform Ramsey and spin-echo experiments [21]. These are interferometric sequences that allow us to measure the phase evolution of a superposition relative to the laser phase.

The Ramsey sequence consists of two laser pulses with duration $\pi/(2\Omega)$ separated by a wait time τ_{R}. First, the ion is prepared in the state $|g\rangle$ and subsequently rotated into a superposition $(|g\rangle + |e\rangle)/\sqrt{2}$ via a resonant pulse $U(\pi/(2\Omega), \Omega, 0, 0)$. The lasers are then turned off for a wait time τ_{R}. During this time the states acquire a phase $\Phi \propto \Delta\tau_{\mathrm{R}}$ relative to each other. The second pulse $U(\pi/(2\Omega), \Omega, 0, \phi)$ transfers the superposition to the excited state, if $\phi = \Phi$. Depending on the phase ϕ the probability to transfer the ion to the excited state is

$$p_e(\phi, \Phi) = \cos^2\left(\frac{\phi - \Phi}{2}\right) \tag{3.9}$$

For $\phi \neq \Phi$ however, the second pulse may lead the ion into a different superposition, or even revert it to its ground state. Thus by varying ϕ we are able to traverse different trajectories on the Bloch sphere and observe oscillations of p_e depending

on ϕ. The state evolution during a Ramsey experiment is visualised in figure 3.3(a).

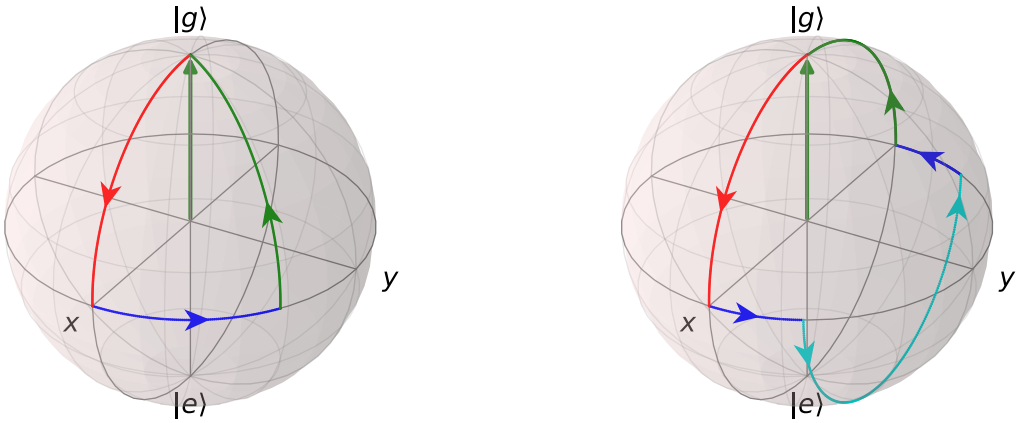

(a) (b)

Figure 3.3: Visualisation of (a) Ramsey and (b) spin-echo sequences on the Bloch sphere. Starting from the ground state (green arrow) the propagator $U(\pi/(2\Omega), \Omega, 0, 0)$ is applied (red line) to rotate the state into the equatorial plane. During a free evolution, indicated by the blue line, the state acquires a phase Φ. In (a) the free evolution ends after a time τ_R and a pulse $U(\pi/(2\Omega), \Omega, 0, \Phi + \pi)$ is applied, transferring the state back to $|g\rangle$. In (b) the free time evolution ends after a time $\tau_\mathrm{R}/2$ a pulse $U(\pi/\Omega, \Omega, 0, 0)$ (cyan line) is applied that exchanges the populations. After another free evolution period $\tau_\mathrm{R}/2$, a pulse $U(\pi/(2\Omega), \Omega, 0, 0)$ rotates the state back to its initial position (green line).

In the experiments presented in section 5.2.2, we use Ramsey sequences to quantify the performance of our setup by applying the sequences multiple times and measure the contrast of equation 3.9. Imperfections in the setup such as magnetic field noise modulate the detuning Δ in time, leading to fluctuations of the acquired phase Φ. This effect is called dephasing and causes decoherence, which manifests itself in a loss of contrast of equation 3.9. Dephasing can also be caused by noise in the laser phase ϕ. As this effect increases with the wait time, we define the coherence time as the time τ_R for which the contrast of $\max(p_e(\phi, \Phi))$ drops to the $1/e$ level. This determines the maximum sequence length, for which we are able to reliably perform qubit operations.

The spin-echo sequence is similar to the Ramsey sequence and can be used to partially compensate for dephasing taking place on time-scales long relative to the sequence length. The sequence, visualised in figure 3.3, starts by creating an equal superposition, followed by a period with no interaction in which one state acquires

the phase Φ. After a time $\tau_R/2$ a pulse $U(\pi/\Omega, \Omega, 0, 0)$ is applied, which transfers the populations between the states $(|g\rangle + e^{i\Phi}|e\rangle)/\sqrt{2} \rightarrow (|e\rangle + e^{i\Phi}|g\rangle)/\sqrt{2}$. During the remaining wait time $\tau_R/2$ the population in $|e\rangle$ again acquires the phase Φ, thus the phase difference between $|e\rangle$ and $|g\rangle$ is compensated. A final pulse $U(\pi/(2\Omega), \Omega, \Delta, 0)$ then transfers the population back to $|g\rangle$. Thus if the fluctuations of Φ are slow compared to τ_R, the spin-echo sequence is able to compensate for them.

Stark Shifts

In a real ion there are multiple excited electronic states that arise, for example, due to the spin-orbit coupling and the Zeeman effect. Therefore, it is also important to consider the effects of off-resonant coupling to these states. Although from equation 3.8 we can see that population transfer with far off-resonant light is unlikely, the ion-light coupling shifts the energy levels of the ion's electronic states. The effect becomes more apparent if we transform the Hamiltonian from equation 3.4 into a frame rotating with $\Delta/2$. We do this by applying a unitary transformation as done in equation 3.4 with the operator $U = \exp(i\Delta t/2)$. This gives us

$$\tilde{H}' = -\frac{\hbar\Delta}{2}\sigma_z - \frac{\hbar\Omega}{2}\left(\sigma_+ e^{i(\phi_L - \Delta t/2)} + \sigma_- e^{-(i\phi_L + \Delta t/2)}\right). \tag{3.10}$$

The eigenstates of this Hamiltonian are superpositions of the ion's initial ground and excited state, called dressed states. The energies of the dressed states are given by the eigenvalues $E_\pm$ of equation 3.10, namely

$$E_\pm = \pm\frac{\hbar}{2}\sqrt{\Delta^2 + \Omega^2} \approx \pm\frac{\hbar|\Delta|}{2} \pm \frac{\hbar\Omega^2}{4|\Delta|}, \tag{3.11}$$

where we expanded the energy under the assumption $|\Delta| \gg |\Omega|$. From equation 3.11 we can see that the energy levels of the ground and excited state are shifted by $\pm\hbar\Omega^2/4|\Delta|$. This shift is called the light-shift or ac-Stark Shift [21]. In section 3.3.1 we describe how one can generate a spatially-varying light-shift using two laser beams. This gives rise to a force that can be used to entangle two ions.

Motional degrees of freedom

In addition to controlling the electronic state of an ion, one can use the ion-light interaction to control the motional states of an ion. We describe the motional states as a harmonic oscillator in the Fock basis $|n\rangle$, where n represents the number of phonons in the motional mode. The coupling of light to the ion's motion is described with the help of the Lamb-Dicke parameter

$$\eta = k_L z_0 = k_L\sqrt{\frac{\hbar}{2m\omega_z}}, \tag{3.12}$$

which relates the laser wavelength to the size of the ground state wave packet z_0 of the harmonic oscillator potential. If the spatial extent of the motional wavefunction is much smaller than the laser wavelength, we enter the Lamb-Dicke regime, i.e. $k_{\mathrm{L}} z_0 \sqrt{\langle n|(a+a^\dagger)^2|n\rangle} \ll 1$. We can then expand the motional exponent from equation 3.3 to first order

$$e^{ik_{\mathrm{L}}z} = e^{i\eta\left(a+a^\dagger\right)} \approx 1 + i\eta\left(a + a^\dagger\right), \tag{3.13}$$

where we used $z = z_0(a + a^\dagger)$ for the position operator. Inserting the expanded exponential into equation 3.3 and applying the RWA after switching into the interaction picture, we find

$$\tilde{H} = -\frac{\hbar\Omega}{2}\left[\sigma_+ e^{i\phi}\left(e^{-i\Delta t} + i\eta\left(a e^{-i(\Delta+\omega)t} + a^\dagger e^{-i(\Delta-\omega)t}\right)\right) + \mathrm{h.c.}\right] \tag{3.14}$$

From this Hamiltonian we find three resonant transitions. For $\Delta = 0$ we find the carrier transition described by

$$\tilde{H}_{\mathrm{C}} = -\frac{\hbar\Omega}{2}\left(\sigma_+ e^{i\phi} + \sigma_- e^{-i\phi)}.\right) \tag{3.15}$$

This transition only changes the electronic state of the ion and does not influence the motional state. For $\Delta = -\omega_z$ we find Hamiltonian for the red sideband

$$\tilde{H}_{\mathrm{RSB}} = -i\frac{\hbar\eta\Omega}{2}\left(a\sigma_+ e^{i\phi} - a^\dagger\sigma_- e^{-i\phi}\right), \tag{3.16}$$

which drives transitions between the states $|g, n\rangle \leftrightarrow |e, n-1\rangle$. Similarly, for $\Delta = \omega_z$ we find the Hamiltonian for the blue sideband transition

$$\tilde{H}_{\mathrm{BSB}} = -i\frac{\hbar\eta\Omega}{2}\left(a^\dagger\sigma_+ e^{i\phi} - a\sigma_- e^{-i\phi}\right). \tag{3.17}$$

This Hamiltonian generates transitions between the levels $|g, n\rangle \leftrightarrow |e, n+1\rangle$. In the Lamb-Dicke Regime the coupling strength to the blue and red sideband scales with $\Omega_{n,n+1} = \eta\sqrt{n+1}\Omega$ and $\Omega_{n,n-1} = \eta\sqrt{n}\Omega$, respectively. For $n = 0$ the ion is in its motional ground state, in which case the red sideband cannot be excited, since no more phonons can be removed from the motional mode. The motional ground state can be reached by means of sideband cooling [14]. However, in the experiment it is often difficult to reach the motional ground state with every experimental trial. Reasons for this include imperfect cooling parameters, limited cooling times to reduce the experimental duration and motional heating [22]. Instead of the ground state, the ion's state is described by a Boltzmann distribution centred around the mean phonon number $\bar{n}$. In our experiment, we use sideband cooling to reach mean phonon numbers on the order of 10^{-2}.

3.2 Three-level atom and Raman interactions

In $^{40}Ca^+$ the $4S_{1/2}$-level consists of two ground states that are not connected via an electric dipole transition since they have the same parity. In principle, one could drive the magnetic dipole transition between these two ground states using microwaves. However, optical light fields offer advantages over microwaves. Due to their shorter wavelength, optical photons can be focused more tightly, allowing for single-ion addressing which offers better scalability. Optical photons also carry a larger momentum than microwaves, thus they couple stronger to the motion of the ions. This is crucial for the entangling gates presented in section 3.3. Raman transitions use a third, excited level to couple the two ground states with optical photons.

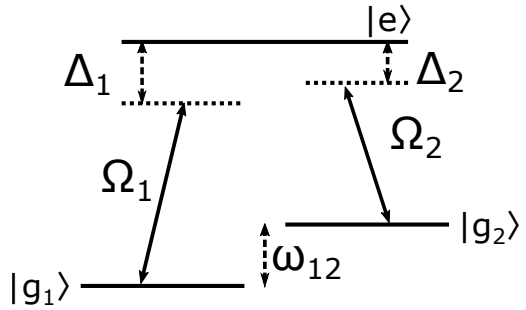

Figure 3.4: Level structure of a three level system used for Raman transitions. The two ground states $|g_1\rangle$ and $|g_2\rangle$ are coupled to the excited state $|e\rangle$ via far-off-resonant laser fields. The lasers are detuned by Δ_1 and Δ_2 with respect to the resonance frequency of the corresponding transition. Setting $\nu = \Delta_2 - \Delta_1 = 0$ corresponds to the lasers being detuned by ω_{12} relative to each other. This allows coherent population transfer between $|g_1\rangle$ and $|g_2\rangle$ without populating $|e\rangle$.

The basic principle of Raman transitions is shown in figure 3.4. The required system consists of an excited state $|e\rangle$ and two ground states $|g_1\rangle$ and $|g_2\rangle$ separated by the energy $\hbar\omega_{12}$. The two ground states $|g_1\rangle$ and $|g_2\rangle$ are coupled to the excited state $|e\rangle$ via the laser fields E_1 and E_2. Each field is characterised by its frequency ω_i, its detuning Δ_i from the excited state $|g_i\rangle$, wavevector $\boldsymbol{k}_i$, phase ϕ_i, Rabi frequency Ω_i and polarisation $\boldsymbol{\epsilon}_i$. Furthermore, we assume that the two ground states are not connected via a dipole transition. Analogous to equation 3.4, in the interaction picture described with the unitary $U = \exp(-\omega_1 |g_1\rangle \langle g_1| - \omega_2 |g_2\rangle \langle g_2|)$ we find the Hamiltonian

$$\tilde{H} = -\frac{\hbar}{2}\left(\Omega_1 e^{i(\boldsymbol{k_1}\cdot\boldsymbol{r}-\Delta_1 t+\phi_1)} |e\rangle \langle g_1| + \Omega_2 e^{i(\boldsymbol{k_2}\cdot\boldsymbol{r}-\Delta_2 t+\phi_2)} |e\rangle \langle g_2| + \text{h.c.}\right) \tag{3.18}$$

As shown in equation 3.8, for large detunings $\Delta_i \gg \Omega_i$ it is unlikely to transfer the ion to the excited state. Thus one can neglect occupation of the excited state and

find an effective Hamiltonian describing the dynamics of the two ground states only. This allows us to simplify the dynamics by eliminating the excited state evolution. One way to do this is to use the James-Jerke approximation, which uses time-averaged dynamics to find an effective Hamiltonian [23]. Assuming that the two detunings are similar $|\Delta_1 - \Delta_2| \ll |\Delta_1|, |\Delta_2|$ we find

$$\tilde{H}_{\text{eff}} = \frac{\hbar\Omega_1^2}{4\Delta_1}\left(|g_1\rangle\langle g_1| - |e\rangle\langle e|\right) + \frac{\hbar\Omega_2^2}{4\Delta_2}\left(|g_2\rangle\langle g_2| - |e\rangle\langle e|\right) + \frac{\hbar\Omega_1\Omega_2}{4\Delta}\left(|g_1\rangle\langle g_2|\, e^{i(\boldsymbol{\delta k}\cdot\boldsymbol{r}-\nu t+\phi)} + |g_2\rangle\langle g_1|\, e^{-i(\boldsymbol{\delta k}\cdot\boldsymbol{r}-\nu t+\phi)}\right) \quad (3.19)$$

with $\phi = \phi_2 - \phi_1$, $\boldsymbol{\delta k} = \boldsymbol{k_2} - \boldsymbol{k_1}$, $\Delta^{-1} = (\Delta_1^{-1} + \Delta_2^{-1})/2$ and $\nu = \Delta_2 - \Delta_1$. The first two terms in equation 3.19 describe constant light-shifts experienced by the respective states. Since they only represent a constant energy shift, but do not change the ion's population, they can be included in the detunings Δ_i to further simplify the Hamiltonian. The third term describes coherent coupling between the two ground state via the two laser fields. It is equivalent to equation 3.4 with the substitutions $\Delta \to \nu$, $\phi_{\text{L}} \to \phi$, $\sigma_+ \to |g_1\rangle\langle g_2|$, $\sigma_- \to |g_2\rangle\langle g_1|$ and $\Omega \to \Omega_{\text{R}}$, with Ω_{R} denoting the Raman Rabi frequency

$$\Omega_{\text{R}} = \frac{\Omega_1\Omega_2}{2\Delta}. \quad (3.20)$$

This shows that the dynamics of the three-level system can be effectively described as a two-level system consisting of the states $|g_1\rangle$ and $|g_2\rangle$. Coherent transfer of population is possible if $\nu \approx 0$, corresponding to the electric fields being detuned by ω_{12} with respect to each other. The difference wavevector $\boldsymbol{\delta k}$ can be chosen by setting the laser beam geometry. In a collinear beam configuration, i.e. $\boldsymbol{\delta k} = 0$, the motion of the ion is unaffected by the lasers, whereas in an orthogonal configuration the $\boldsymbol{\delta k}$ can be chosen to be parallel to the axial motional mode, thus allowing control of the ion's axial motion.

Raman transitions in this work are implemented between the Zeeman sublevels of the state $4S_{1/2}$-manifold for $^{40}\text{Ca}^+$. Here, the sublevels of the $4P_{1/2}$- and $4P_{3/2}$-manifolds act as intermediate, excited states. In the following we will use the notation $|4S_{1/2}, m_j = -1/2\rangle = |\downarrow\rangle$ and $|4S_{1/2}, m_j = 1/2\rangle = |\uparrow\rangle$. One has to account for all sublevels of the excited state manifolds to find the correct Raman Rabi frequency. By summing over the transition elements of all the intermediate states $|e\rangle$, we find

$$\Omega_{\text{R}} = \sum_{J\in\{\frac{1}{2},\frac{3}{2}\}}\sum_{e}\frac{\langle\downarrow|\, E_2\boldsymbol{\epsilon_2}\cdot\boldsymbol{d}\,|e\rangle\langle e|\, E_1\boldsymbol{\epsilon_1}\cdot\boldsymbol{d}\,|\uparrow\rangle}{2\Delta_J}, \quad (3.21)$$

where J represents the total angular momentum quantum number of the corresponding $4P_{1/2}$- or $4P_{3/2}$-manifold with Zeeman sublevels $|e\rangle$ and Δ_J the detuning

from the respective manifold. Equation 3.21 shows that due to the structure of the excited states, one has to choose the correct polarisations to satisfy the selection rules and obtain Raman coupling between the ground states. Here, it is convenient to describe the polarisation vector $\boldsymbol{\epsilon}$ of the light field in the basis $\{\sigma^+, \pi, \sigma^-\}$, where σ^+ and σ^- components drive transitions with change in magnetic quantum number $\Delta m_j = \pm 1$ and the π component transitions with $\Delta m = 0$. In this basis, it is important to consider the direction of the wavevector $\boldsymbol{k}$ and the magnetic field $\boldsymbol{B}$. For $\boldsymbol{k} \parallel \boldsymbol{B}$, σ^+ and σ^- correspond to right- and left-handed circularly polarised light. A linearly polarised beam along $\boldsymbol{B}$ can be described as a superposition of right- and left-handed circularly polarised light, therefore it consists of equal amounts of σ^+ and σ^-. We denote this polarisation as $\sigma^\pm = \{1, 0, 1\}$. For $\boldsymbol{k} \perp \boldsymbol{B}$ we find two important cases for linearly polarised beams. If $\boldsymbol{\epsilon} \parallel \boldsymbol{B}$, the beam is π-polarised. For $\boldsymbol{\epsilon} \perp \boldsymbol{B}$, the beam is again $\sigma^\pm$-polarised.

If both beams are either only $\sigma^\pm$ or only π polarised, the Raman coupling between the ground states vanishes and the beam pair only induces a light-shift on the states. Similar to equation 3.21, the total light-shift on the $|\uparrow\rangle$ state induced by the Raman beam pair is given by

$$\Omega_\uparrow = \sum_{J \in \{\frac{1}{2}, \frac{3}{2}\}} \sum_e \frac{\langle\uparrow| E_2 \boldsymbol{\epsilon_2} \cdot \boldsymbol{d} |e\rangle \langle e| E_1 \boldsymbol{\epsilon_1} \cdot \boldsymbol{d} |\uparrow\rangle}{2\Delta_J}, \tag{3.22}$$

and analogously for the $|\downarrow\rangle$ state. Setting the beam pair's polarisations to $\sigma^\pm = \{1, 0, 1\}$ and $\sigma^\mp = \{1, 0, -1\}$ results in opposite signs for $\Omega_\uparrow$ and $\Omega_\downarrow$, thus creating a spin-dependent light-shift. This is used to create the entangling gate operation described in section 3.3.1. In section 4.2.3 we describe how we set the beams to the necessary polarisation.

3.3 Two-Qubit operations

So far we have only discussed ion-light interactions that allow us to control the state of single qubits independently. In this section we present two methods on how Raman beams can be used to entangle two ions. For the first method, we follow the approach from ref. [24, 25] to show how a spin-dependent light-shift can be used to implement a two-qubit gate in the $(\sigma_z \otimes \sigma_z)$ basis. The second method uses a bichromatic modulation of one of the beams to create a $(\sigma_x \otimes \sigma_x)$-interaction similar to the commonly used Mølmer-Sørensen gate introduced in ref. [26].

3.3.1 The light-shift gate

Creating a spin-dependent force can be realised by using spatially varying single-qubit light-shifts induced by a pair of orthogonal Raman beams as seen in figure 3.5(a). Instead of coupling the two ground states, choosing the polarisations of the

Raman beam pair to be $\sigma^{\pm}$ and $\sigma^{\mp}$ only induces a light-shift on each state according to equation 3.22. The superposition of the two beams creates a standing wave pattern with periodically varying polarisations along the difference wavevector $\boldsymbol{\delta k}$. The frequency difference between the Raman beams will be set close to the axial COM mode frequency ω_z. Analogous to equation 3.4 the Hamiltonian in the interaction picture reads

$$\tilde{H} = \sum_{s=\uparrow,\downarrow} -\frac{\hbar\Omega_{1,s}}{2} |e\rangle \langle s| e^{i(\boldsymbol{k_1}\cdot\boldsymbol{r}-\Delta_{1,s}t+\phi_1)} - \frac{\hbar\Omega_{2,s}}{2} |e\rangle \langle s| e^{i(\boldsymbol{k_2}\cdot\boldsymbol{r}-\Delta_{2,s}t+\phi_2)} + \text{h.c.}, \quad (3.23)$$

where $\Omega_{1,s}$ denotes the coupling of the first beam to the spin state $|s\rangle$ and analogously for $\Omega_{2,s}$. It should be noted that the detunings $\Delta_{1,s}$ and $\Delta_{2,s}$ both represent the detuning with respect to the frequency of the $|s\rangle \leftrightarrow |e\rangle$-transition. Applying the James-Jerke approximation to equation 3.23 yields time-dependent and time-independent light-shifts with no coupling between the states $|g_1\rangle$ and $|g_2\rangle$. Again, the time-independent Stark-Shifts can be absorbed into the detuning and we find for the ground states

$$\tilde{H} = \sum_{s=\uparrow,\downarrow} -\frac{\hbar\Omega_{1,s}\Omega_{2,s}}{4\Delta} |s\rangle \langle s| e^{i(\boldsymbol{\delta k}\cdot\boldsymbol{r}-\nu t+\phi)} + \text{h.c.}, \quad (3.24)$$

with $\Delta^{-1} = (\Delta_{1,s}^{-1} + \Delta_{2,s}^{-1})/2$ and $\nu = \Delta_{2,s} - \Delta_{1,s}$. This interaction does not change the population of the ion, but instead only induces a phase shift on the state $|s\rangle$, which oscillates with the detuning ν and depends on the light-shift amplitude. The phase term $\exp(i\boldsymbol{\delta k}\cdot\boldsymbol{r})$ describes a spatially varying light-shift, visualised in figure 3.5(b), that gives rise to a force. For beam polarisations $\sigma^{\pm}$ and $\sigma^{\mp}$ the light-shifts on the states $|\downarrow\rangle$ and $|\uparrow\rangle$ have opposite sign, thus creating a spin-dependent force.

When using two beams, the Lamb-Dicke factor depends on the geometry of the beams relative to the axis of the motional mode. In our experiment the wavelength difference between the two beams ($\approx 10^{-15}\,\text{m}$) is much smaller than their absolute wavelength ($\approx 10^{-7}\,\text{m}$), thus we can assume $|\boldsymbol{k}_1| = |\boldsymbol{k}_2|$ and find $|\boldsymbol{\delta k}| = 2|\boldsymbol{k}_1|\sin(\varphi/2)$, where φ denotes the angle between the two beams. Considering only the axial COM mode, we find the product $\boldsymbol{\delta k}\cdot\boldsymbol{r} = \eta(a + a^{\dagger})$ with the Lamb-Dicke factor

$$\eta = \boldsymbol{\delta k}\cdot\boldsymbol{r} = 2|\boldsymbol{k}_1| z_0 \sin\left(\frac{\varphi}{2}\right)\cos(\vartheta), \quad (3.25)$$

where ϑ denotes the angle between $\boldsymbol{\delta k}$ and the axial trap direction. In this work we use an orthogonal beam pair with its difference wavevector aligned along the z-axis, resulting in $\varphi = \pi/2$ and $\vartheta = 0$.

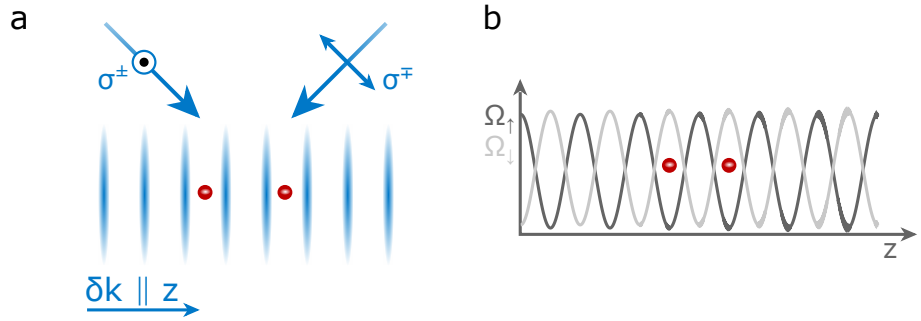

Figure 3.5: Creating a spin-dependent force with two Raman beams. (a) Two beams with linear polarisations $\sigma^{\pm}$ and $\sigma^{\mp}$ create a standing wave pattern with periodically varying polarisations along $\boldsymbol{\delta k} \parallel z$. (b) This results in a spatially varying light-shift that generates a spin-dependent force with opposite sign for the states $|\downarrow\rangle$ and $|\uparrow\rangle$.

Next we expand equation 3.24 in the Lamb-Dicke regime to $\exp(i\boldsymbol{\delta k}\cdot\boldsymbol{r}) \approx 1 + i\eta(a + a^{\dagger})$ and include the time-dependent exponents of the motional operators by switching into the interaction picture with respect to the motional states. We find

$$\tilde{H} = \sum_{s=\uparrow,\downarrow} -\frac{\hbar\Omega_s}{2} |s\rangle\langle s| \Big[2\cos(\nu t - \phi) + i\eta\Big(ae^{i(-(\nu+\omega_z)t+\phi)} + a^{\dagger}e^{i((-\nu+\omega_z)t+\phi)} - ae^{-i(-(\nu-\omega_z)t+\phi)} - a^{\dagger}e^{-i(-(\nu+\omega_z)t+\phi)}\Big)\Big], \quad (3.26)$$

where we defined $\Omega_s = \Omega_{1,s}\Omega_{2,s}/(2\Delta)$. Here, the first term describes a time-dependent light-shift that leads to a single-qubit phase. However, the error caused by this is negligible if $\Omega \ll \nu$ and can be further suppressed by using pulse-shaping [25]. Therefore, we can eliminate this term. The terms $\propto \eta$ generate a harmonic driving force on the ion's motional state. Setting $\nu = \omega_z + \delta_g \approx \omega_z$, allows us to eliminate the rotating terms with $\delta_g + \omega_z$ under the RWA, resulting in

$$\tilde{H} = \sum_{s=\uparrow,\downarrow} \frac{\hbar\Omega_s}{2} i\eta |s\rangle\langle s| \left(ae^{i(\delta_g t+\phi)} - a^{\dagger}e^{-i(\delta_g t+\phi)}\right). \quad (3.27)$$

By integrating this Hamiltonian and applying the Magnus expansion [27] we find the propagator

$$U(t) = \left(\sum_{s=\uparrow,\downarrow} D(\alpha_s) |s\rangle\langle s|\right) e^{-i\Phi}, \quad (3.28)$$

with

$$\alpha_s = -\frac{\Omega_s \eta}{\delta_g} e^{i\phi} e^{-i\delta_g t/2} \sin\left(\frac{\delta_g t}{2}\right), \tag{3.29}$$

$$\Phi = \frac{\eta^2}{4\delta_g^2} \left(\delta_g t - \sin(\delta_g t)\right) \left(\sum_{s=\uparrow,\downarrow} \Omega_s \left|s\right\rangle \left\langle s\right|\right)^2. \tag{3.30}$$

and $D(\alpha_s) = \exp(\alpha_s a^\dagger - \alpha_s^* a)$ denoting the displacement operator [28].

We can separate the effects of this propagator into a motional part and an internal, electronic part. Applying $D(\alpha_s)$ causes a displacement in motional phase space proportional to Ω_s. Since Ω_s depends on the ion's electronic state, the displacement α_s is spin-dependent. With this we are able to create a spin-dependent force on the motional state. As discussed in section 3.2, we can choose the beam polarisations to obtain $\Omega_\downarrow = -\Omega_\uparrow$, which creates opposite displacement for $|\downarrow\rangle$ and $|\uparrow\rangle$. If $\delta_g \neq 0$, the ion's motion is periodically excited and deexcited with period $\sin(\delta_g t/2)$. This behaviour can be visualised as loops in motional phase space as seen in figure 3.6. Due to the interaction, the initial state $|s\rangle \otimes |0\rangle$ is excited to a coherent state $e^{i\Phi(t)} |s\rangle \otimes |\alpha_s(t)\rangle$, leading to spin-motion entanglement. After $t_g = 2\pi/\delta_g$, the ion returns to its initial motional state, disentangling spin and motion. The resulting state $e^{i\Phi(t_g)} |s\rangle \otimes |0\rangle$ will have acquired the phase $\Phi(t_g)$. The phase Φ depends on area enclosed by the loop and is therefore called the geometric phase.

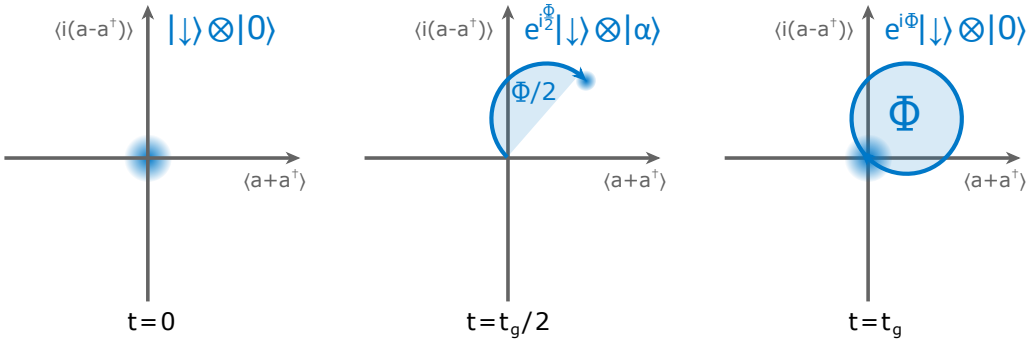

Figure 3.6: Displacing the ion in phase space. At $t = 0$ the ion is prepared in the state $|\downarrow\rangle \otimes |0\rangle$, located at the origin of motional phase-space. By applying equation 3.28 the ion is displaced along a circular trajectory, which entangles spin and motion by creating the state $e^{i\Phi(t)} |\downarrow\rangle \otimes |\alpha\rangle$. After a time $t_g = 2\pi/\delta_g$, the ion returns to its motional ground state, closing the loop in phase space and having acquired the phase Φ.

By changing the beam power and polarisation we are able to tune the magnitude and sign of Ω_s and are therefore able to control Φ. If $\Omega_\uparrow = \Omega_\downarrow$, the operator

$\sum \Omega_s |s\rangle \langle s|$ from equation 3.30 would be the identity and have no effect on the ion's electronic state, as it only imprints a global phase. As described in equation 3.22, by changing the beam polarisations we are able to tune $\Omega_\uparrow$ and $\Omega_\downarrow$. Thus we are able to modify the elements of $\sum \Omega_s |s\rangle \langle s|$, allowing us to control the geometric phase that each state acquires. Setting the Raman beam polarisations to $\sigma^\pm$ and $\sigma^\mp$ leads to $\Omega_\uparrow = -\Omega_\downarrow$, hence $\sum \Omega_s |s\rangle \langle s|$ becomes the σ_z operator. This configuration will be used for two ions to create a state-dependent force that is used to entangle the ions.

Up to now, we have only considered the effect of the light-shift force on a single ion. The interaction from equation 3.27 can be readily extended to two ions. Each ion's electronic states are described by $|s\rangle_j$, where j denotes the ion number. Although there are two axial motional modes for two ions, we only consider the axial center of mass mode, since ν can be detuned sufficiently far from the breathing mode. From this we find the Hamiltonian

$$\tilde{H} = \sum_{j=1,2} \frac{i\hbar\eta}{2} \left(\Omega_\uparrow |\uparrow\rangle_j \langle\uparrow| + \Omega_\downarrow |\downarrow\rangle_j \langle\downarrow| \right) a e^{i(\delta_g t + \phi + \phi_{z,j})} + \text{h.c.}, \tag{3.31}$$

where we introduced the phase term $\phi_{z,j}$ that describes the phase of the light-shift force the ions experience relative to each other. For simplicity, we can set $\phi_{z,1} = 0$ and $\phi_{z,2} = \phi_z$, where $\phi_z = \delta k \Delta z$ is determined by the ion's equilibrium spacing Δz. We can tune this phase by adjusting the ion spacing relative to the standing wave pattern created by the Raman beams. As described in equation 2.17, the spacing between two ions depends only on the motional frequency, and can thus be varied by changing the static voltage applied to the electrodes.

By integrating equation 3.31, one finds the propagator similar to equation 3.28, with the σ_z operator from equation 3.30 being expanded to the case of two ions. The diagonal elements of this operator are

$$|\uparrow\uparrow\rangle \to \Omega_\uparrow(1 + e^{i\phi_z}) \tag{3.32}$$

$$|\uparrow\downarrow\rangle \to \Omega_\uparrow + \Omega_\downarrow e^{i\phi_z} \tag{3.33}$$

$$|\downarrow\uparrow\rangle \to \Omega_\downarrow + \Omega_\uparrow e^{i\phi_z} \tag{3.34}$$

$$|\downarrow\downarrow\rangle \to \Omega_\downarrow(1 + e^{i\phi_z}). \tag{3.35}$$

They describe the light-shift force experienced by the different states and therefore determine the acquired phase of each state.

After applying the gate interaction for a time t_g, the loops in phase space are closed and states will have acquired the geometric phases

$$\Phi_{\text{even}} = \frac{\eta^2 t_g}{4\delta_g} \left(\Omega_\uparrow + e^{i\phi_z} \Omega_\uparrow \right)^2, \tag{3.36}$$

$$\Phi_{\text{odd}} = \frac{\eta^2 t_g}{4\delta_g} \left(\Omega_\uparrow + e^{i\phi_z} \Omega_\downarrow \right)^2, \tag{3.37}$$

where Φ_{even} denotes the phase acquired by $|\uparrow\uparrow\rangle$ and $|\downarrow\downarrow\rangle$, and Φ_{odd} the phase acquired by $|\uparrow\downarrow\rangle$ and $|\uparrow\downarrow\rangle$. The phase difference between the states $|\uparrow\uparrow\rangle$ and $|\uparrow\downarrow\rangle$ is then

$$\Phi = \Phi_{\text{odd}} - \Phi_{\text{even}} = \frac{\eta^2 t_{\text{g}}}{4\delta_{\text{g}}} \left[\left(\Omega_\uparrow + e^{i\phi_z} \Omega_\downarrow \right)^2 - \left(\Omega_\uparrow + e^{i\phi_z} \Omega_\uparrow \right)^2 \right]. \tag{3.38}$$

For a given gate time, the laser power can be chosen to obtain $\Phi = \pi/2$, yielding the propagator for the phase gate

$$U_{\text{phase}} = \text{diag}(1, i, i, 1). \tag{3.39}$$

As this operator acts in the $(\sigma_z \otimes \sigma_z)$-basis, it does not change the population of the ion's electronic state. However, it can be embedded in a Ramsey or spin-echo sequence to entangle two ions. Applying the sequence $G = R_x^{(2)}(\pi/2) U_{\text{phase}} R_x^{(2)}(\pi/2)$ on the initial state $|\downarrow\downarrow\rangle$ creates the Bell state $|\Phi^+\rangle$, with $R_x^{(2)}(\pi/2) = R_x(\pi/2) \otimes R_x(\pi/2)$. This sequence can also be expanded to incorporate a spin-echo sequence, as will be demonstrated in section 5.3.4. Although an additional π-pulse is needed for the spin-echo sequence, it has the advantage of cancelling single-qubit phases acquired during the Ramsey sequence.

From equations 3.32-3.35 we see that the force on each state is determined by ϕ_z. As $\phi_z = \delta k \Delta z$ depends on the distance Δz between the ions, we are able to create a state-selective force by varying the ion spacing. For $\phi_z = \pi$ there is no net force acting on the motion of the states $|\uparrow\uparrow\rangle$ and $|\downarrow\downarrow\rangle$. Therefore, during the gate sequence G, only the motion of the states $|\downarrow\uparrow\rangle$ and $|\uparrow\downarrow\rangle$ is excited and they acquire a geometric phase. This is desired, since it maximises the phase difference Φ from equation 3.38 for any given beam power, hence making the gate more efficient. In section 5.3.1 we demonstrate how the spacing can be set to obtain $\phi_z = \pi$.

3.3.2 Raman Mølmer-Sørensen gate

A different method to implement an entangling gate is to use Raman interactions to create a $(\sigma_x \otimes \sigma_x)$ interaction. This is equivalent to the commonly used Mølmer-Sørensen (MS) gate first described in ref. [26].

Similar to the geometric phase gate, the Raman $(\sigma_x \otimes \sigma_x)$ interaction uses two orthogonal laser beams interacting with a three-level system as seen in figure 3.7. Similar to the Raman interactions discussed in section 3.2, one beam with wavevector $\boldsymbol{k}_1$ and phase ϕ_1 couples to the $|g_1\rangle \leftrightarrow |e\rangle$ transition with strength Ω_1 and detuning Δ_1. A second beam with $\boldsymbol{k}_2 \perp \boldsymbol{k}_1$ is detuned by Δ_2 from the $|g_2\rangle \leftrightarrow |e\rangle$ transition, with coupling strength Ω_2. Note that this couples the two ground states via Raman interactions and creates an effective two-level system as described in section 3.2. For $\Delta_2 = \Delta_1$ the frequency difference between the two beams matches

the frequency difference between the states $|g_1\rangle$ and $|g_2\rangle$, creating resonant interactions between the two ground states. As shown in figure 3.7, the second beam consists of two spectral components detuned by $\Delta_\mathrm{b} = \Delta_1 + \omega_z + \delta_\mathrm{g}$ and $\Delta_\mathrm{r} = \Delta_1 - \omega_z - \delta_\mathrm{g}$ from the $|g_2\rangle \leftrightarrow |e\rangle$ transition. The two components couple to the blue and red sidebands with coupling strength $\Omega_{2,\mathrm{b}}$ and $\Omega_{2,\mathrm{r}}$, respectively.

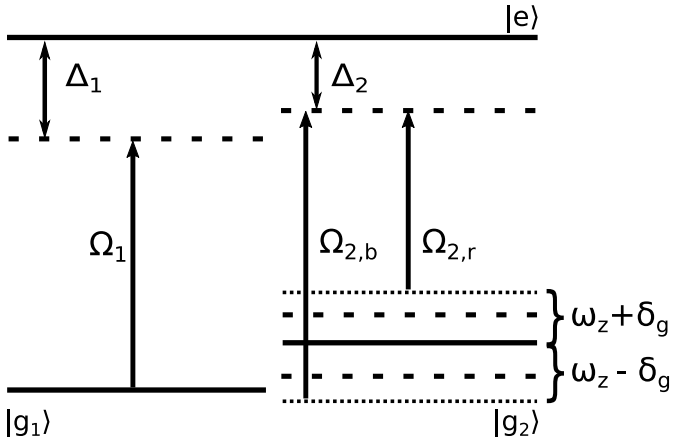

Figure 3.7: Level and laser diagram used for the Raman MS gate. One laser couples with strength Ω_1 to the $|g_1\rangle - |e\rangle$ transition, from which it is detuned by Δ_1. The states $|g_2\rangle$ and $|e\rangle$ are coupled via a second laser, which is modulated with a bichromatic field. The two components $\Omega_{2,\mathrm{b}}$ and $\Omega_{2,\mathrm{r}}$ are detuned from the $|g_2\rangle - |e\rangle$ transition by $\Delta_1 + \omega_z + \delta_\mathrm{g}$ and $\Delta_1 - \omega_z - \delta_\mathrm{g}$ respectively.

Each component of the bichromatic field generates an interaction as described in equation 3.19, with the substitution $\Omega_2 \to \Omega_{2,\mathrm{i}}$ and for $\phi \to \phi_\mathrm{i}$ $i = \mathrm{r}, \mathrm{b}$. Summing the interactions and applying the Lamb-Dicke approximation, we find

$$\begin{aligned}\tilde{H}_\mathrm{eff} = &\frac{\hbar\Omega_1\Omega_{2,\mathrm{r}}}{4\Delta}\,|g_1\rangle\langle g_2|\left[e^{i(\omega_z+\delta_\mathrm{g})t} + i\eta\left(ae^{i\delta_\mathrm{g}t} + a^\dagger e^{i(2\omega_z+\delta_\mathrm{g})t}\right)\right]e^{i\phi_\mathrm{r}} \\ &+ \frac{\hbar\Omega_1\Omega_{2,\mathrm{b}}}{4\Delta}\,|g_1\rangle\langle g_2|\left[e^{-i(\omega_z+\delta_\mathrm{g})t} + i\eta\left(ae^{-i(2\omega_z+\delta_\mathrm{g})t} + a^\dagger e^{-i\delta_\mathrm{g}t}\right)\right]e^{i\phi_\mathrm{b}} + \mathrm{h.c.}\,.\end{aligned} \tag{3.40}$$

Here, ϕ_r and ϕ_b describe the phase of the first beam relative to the red and blue detuned component, respectively. For $\delta_\mathrm{g}, \Omega_i \ll \omega_z$ we can use the RWA and eliminate the carrier term and the fast sideband terms with $2\omega_z + \delta_g$ as done for equation 3.27. By equalising the Rabi frequency of the two components, i.e. $\Omega_\mathrm{sb} = \Omega_{2,\mathrm{r}} = \Omega_{2,\mathrm{b}}$ we find

$$\tilde{H} = \frac{\hbar\Omega_1\Omega_{2,\mathrm{sb}}\eta}{4\Delta}\sigma_\phi\left(ae^{i(\delta_\mathrm{g}t-\phi_\mathrm{m})} + a^\dagger e^{-i(\delta_\mathrm{g}t-\phi_\mathrm{m})}\right), \tag{3.41}$$

where $\phi_\mathrm{m} = (\phi_\mathrm{b} - \phi_\mathrm{r})/2$ and $\sigma_\phi = ie^{i\phi_\mathrm{s}} |g_1\rangle\langle g_2| - ie^{-i\phi_\mathrm{s}} |g_2\rangle\langle g_1|$ with $\phi_\mathrm{s} = (\phi_\mathrm{b} + \phi_\mathrm{r})/2$. For simplicity, we will continue with the assumption $\phi_\mathrm{s} = -\pi/2$, resulting in the operator σ_ϕ becoming the σ_x operator with eigenstates $|+\rangle$ and $|-\rangle$.

Since equation 3.41 is equivalent to equation 3.27, we can integrate it using a Magnus expansion, yielding the propagator

$$U(t) = \Big[D(\alpha)\,|+\rangle\langle+| + D(-\alpha)\,|-\rangle\langle-|\,\Big]e^{-i\Phi}, \tag{3.42}$$

with

$$\alpha = -\frac{\eta\Omega_\mathrm{MS}}{\delta_g} e^{i\phi_\mathrm{m}} e^{-i\delta_g t/2} \sin\left(\frac{\delta_g t}{2}\right), \tag{3.43}$$

$$\Phi = -\frac{\eta^2\Omega_\mathrm{MS}^2}{4\delta_g^2}\left(\delta_g t - \sin(\delta_g t)\right)\sigma_x^2, \tag{3.44}$$

where we defined $\Omega_\mathrm{MS} = \Omega_1\Omega_{2,\mathrm{sb}}/(2\Delta)$. Applying this propagator to a single ion in the ground state creates a coherent motional state by driving loops in phase-space. Contrary to the light-shift gate, when applied to either $|g_1\rangle$ or $|g_2\rangle$, this interaction also changes the population of the ion's electronic states, since the Hamiltonian acts in the σ_x basis.

Generalising equation 3.41 to the case of two ions is straightforward and yields the MS gate interaction commonly used in trapped ion experiments. Defining the operators $\sigma_{x,1} = \sigma_x \otimes \mathbb{1}$ and $\sigma_{x,2} = \mathbb{1} \otimes \sigma_x$, we find

$$\tilde{H}_\mathrm{MS} = \sum_{j=1,2} \frac{\hbar\eta\Omega_\mathrm{MS}}{2}\sigma_{x,j}\left(ae^{i(\delta_\mathrm{g}t-\phi_\mathrm{m})} + a^\dagger e^{-i(\delta_\mathrm{g}t-\phi_\mathrm{m})}\right). \tag{3.45}$$

Integrating equation 3.45, one finds the propagator similar to equation 3.42, with the σ_x operator from equation 3.44 being expanded to the case of two ions, i.e. $\sigma_x^2 \to (\sigma_{x,1} + \sigma_{x,2})^2 \propto (\mathbb{1} + \sigma_{x,1}\sigma_{x,2})$. From this, one can see that this operator acts in the $(\sigma_x \otimes \sigma_x)$ basis. For a closed phase-space loop and $\Phi = \pi/2$, this interaction yields the operator

$$U_\mathrm{MS} = \frac{1}{\sqrt{2}}\begin{pmatrix} 1 & 0 & 0 & -i \\ 0 & 1 & -i & 1 \\ 0 & -i & 1 & 0 \\ -i & 0 & 0 & 1 \end{pmatrix}. \tag{3.46}$$

Applying this to two ions in the state $|\downarrow\downarrow\rangle$ creates the state $|\uparrow\uparrow\rangle - i\,|\downarrow\downarrow\rangle$. In section 5.4 we demonstrate entanglement of two $^{40}\mathrm{Ca}^+$ ions using this interaction.

We now want to discuss the similarities and differences between the phase gate Hamiltonian from equation 3.27 and equation 3.41. Both interactions drive loops

in motional phase-space with period $2\pi/\delta_g$ and thus periodically create and annihilate a coherent motional state. The main difference consists of the phase gate Hamiltonian acting in the $(\sigma_z \otimes \sigma_z)$-basis of the electronic states, whereas the MS-Hamiltonian acts in the $(\sigma_x \otimes \sigma_x)$-basis. Hence, for two ions, contrary to the phase gate, the MS gate interaction does not require additional $\pi/2$ rotations to create an entangled state. The phase gate operation bears the advantage that it is independent of the qubit frequency, which makes it more suitable when working with ions with different transition frequencies. This property makes the light-shift gate suitable for entangling ions of two different atomic species with high fidelity [29].

3.4 Trapped $^{40}Ca^+$ ions as qubits

Qubit operations in this work have been performed on trapped $^{40}Ca^+$ ions. The level scheme of $^{40}Ca^+$ is shown in figure 3.8. The relevant levels in this thesis are the $4S_{1/2}$ ground state, the $4P_{1/2}$ and the $4P_{3/2}$ excited states as well as the metastable $3D_{3/2}$ and $3D_{5/2}$ excited states. Due to their non-existent nuclear spin $I = 0$, $^{40}Ca^+$ ions exhibit no hyperfine structure.

The trapping process starts with the emission of neutral ^{40}Ca atoms from an oven. The neutral ^{40}Ca atoms are then ionised at the trap centre with light from a 422 nm and a 375 nm laser. This two-step photoionisation process is isotope selective. The ions are then Doppler-cooled using 397 nm light, red detuned by ≈ 20 MHz from the $4S_{1/2} \leftrightarrow 4P_{1/2}$ transition. This transition is used for Doppler cooling due to its lifetime of $\tau \approx 7$ ns [30]. Since there is a 6 % [31] chance for the state to decay into the $D_{3/2}$ state, an 866 nm beam is kept on to transfer the ions back into the $4P_{1/2}$ state and maintain the cooling cycle.

Before performing quantum logic operations, the ion is initialised in the state $|4S_{1/2}, m_j = -1/2\rangle$ via optical pumping. This is done by first transferring the ion to the $|3D_{5/2}, m_j = -5/2\rangle$ state and subsequently to the $|3P_{3/2}, m_j = -3/2\rangle$, which eventually decays to the $|4S_{1/2}, m_j = -1/2\rangle$ state. Afterwards, sideband cooling is used to initialise the ion in its motional ground state. For this, the ion is first excited to the $3D_{5/2}$ on the red sideband and subsequently excited to the $4P_{3/2}$ level, as this state decays faster to the ground state than the metastable $3D_{5/2}$ level.

The state of the ion is read out using a fluorescence measurement consisting of continuously illuminating the ion with light resonant with the $4S_{1/2} \leftrightarrow 4P_{1/2}$ transition. Fluorescence is observed if the ion is in the state $4S_{1/2}$, whereas no fluorescence is observed if the ion is in the state $3D_{5/2}$. Using a fluorescent measurement, readout fidelities of 99.991 % have been demonstrated [32].

Performing quantum logic operations requires one to first choose the computational basis. For $^{40}Ca^+$ there are two commonly used computational bases. The

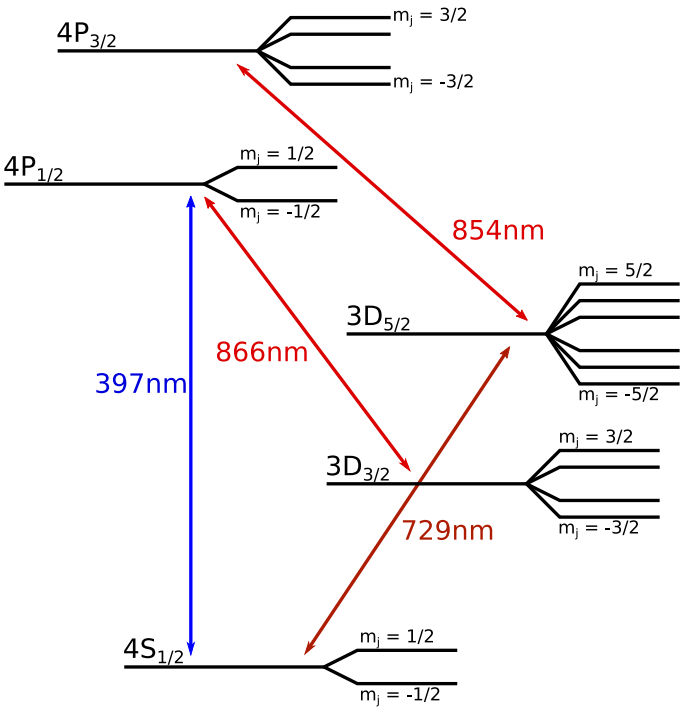

Figure 3.8: Level Scheme of $^{40}Ca^{+}$. The ground state qubit is encoded in the two Zeeman sublevels of the $4S_{1/2}$ manifold. Doppler cooling and readout are performed on the $4S_{1/2} \leftrightarrow 4P_{1/2}$ transition, while the 866 nm laser is continuously kept on for repumping. Optical pumping and sideband cooling is performed on the $4S_{1/2} \leftrightarrow 3D_{5/2}$ transition. Upon being excited to the $3D_{5/2}$ states, the ion is excited to the state $4P_{3/2}$ and subsequently decays to the state $|4S_{1/2}, m_j = -1/2\rangle$.

first is the optical qubit, where the two qubit states are encoded in the $4S_{1/2}$ and the $3D_{5/2}$ manifold. The metastable $3D_{5/2}$-level is suitable for quantum computations due to its lifetime of $\tau = 1.168\,\mathrm{s}$ [33] compared to the duration of qubit operations on the order of 10 µs. To date, quantum operations on the $^{40}Ca^{+}$ optical qubit have been performed with fidelities of up to 99.995 % [34] for single-qubit and 99.6 % [35] for two-qubit operations.

In this work we focus on operations on the ground state qubit, defined by the two Zeeman sublevels $|4S_{1/2}, m_j = 1/2\rangle = |\uparrow\rangle$ and $|4S_{1/2}, m_j = -1/2\rangle = |\downarrow\rangle$. Contrary to the optical qubit, the ground state qubit in principle offers unlimited qubit lifetime, though the coherence time is often limited by magnetic field fluctuations. The linear Zeeman effect splits the two ground states by 2.802 41 MHz/G [36]. The magnetic field strength of $B = 3.66\,\mathrm{G}$ used in our setup generates a qubit splitting of $\approx 10\,\mathrm{MHz}$, which is smaller than the natural linewidth $\Gamma = 22\,\mathrm{MHz}$ of the $4s_{1/2} \leftrightarrow 4P_{1/2}$ transition. This makes it impossible to discriminate the state via a simple fluorescence measurement. We circumvent this by electron shelving,

i.e. transferring the $|\uparrow\rangle$ state to the $3D_{5/2}$ level via a resonant laser pulse. By using Raman interactions, single-qubit and two-qubit fidelities of 99.995 % and 99.1 % have been achieved with $^{40}Ca^{+}$ ions [37].

4 Experimental Setup & Characterization

4.1 Trap setup and Control

The ion trap used for this thesis is a segmented linear surface trap contained in a cryogenic setup that was designed to build a platform for scalable quantum computation. A detailed description of the trap setup can be found in ref. [38], this thesis only summarises fundamental components of the setup.

The trap, shown in figure 4.1, consists of 27 individually controllable electrode pairs, a central rf electrode pair and a split central electrode. The two central electrodes are separated by a slit. Individual electrodes are separated by trenches etched to a depth of $\approx 40\,\mu m$. Multiple electrode pairs are used to create a harmonic trapping potential 100 µm above the surface, at a desired location along the slit.

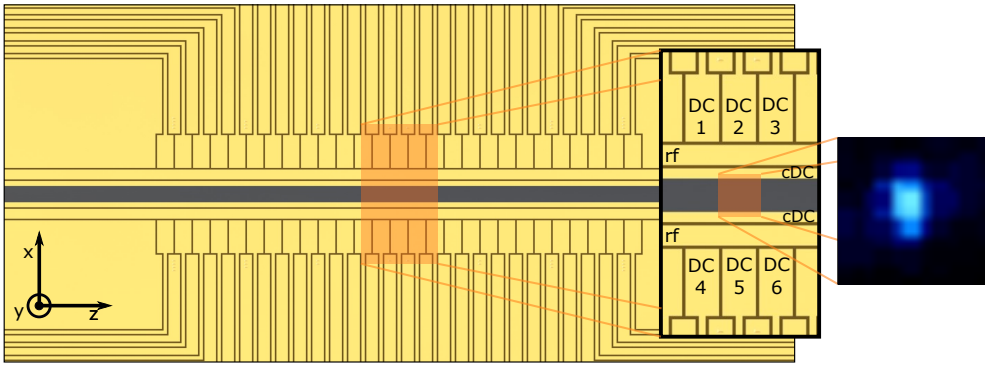

Figure 4.1: Schematic of the segmented surface trap used in this work. Ions are trapped via potentials created by the static electrode pairs (DC1-DC6), a central rf electrode pair (rf), and a split static center electrode (cDC). The ion (blue dot) is trapped 100 µm above the slit.

The trap setup is contained in a liquid Helium flow cryostat. Inside the cryostat, the trap is surrounded by an outer heat shield and an inner heat shield made out of copper. The inner heat shield is connected to the cryostat's coldfinger. The coldfinger is cooled down to 15 K, such that the inner heat shield reaches 35 K. The cryogenic environment reduces collision rates with background gas and the average collision energy, thus increasing the ion's lifetime inside the trap. Moreover, the cryogenic environment reduces the heating rates on the ion's motional modes, which also lowers the gate error due to motional heating.

The magnetic field defining the quantisation axis is created by a pair of Helmholtz coils with the magnetic field vector being at a 45° angle with respect to the axial trap direction, which is labelled as z-axis in figure 4.1. Environmental influences such as the Earth's magnetic field as well as noise in the Helmholtz

coil's current create magnetic field noise that modulate the qubit frequency in time and eventually lead to decoherence. Therefore, we monitor magnetic field noise with two sensors placed along the quantisation axis. Three pairs of cable loops surrounding the trap table are oriented along all three spatial dimensions to actively compensate magnetic field fluctuations by modulating the current through the coils.

Eight viewports in the vacuum chamber grant optical access to the trap and are used to guide lasers to the trap. A detailed description of the Raman beam layout is discussed in section 4.2.3. Additionally, a 0.23 NA in-vacuum lens is used to collect fluorescence light. The fluorescence light is then guided through a viewport to either a photomultiplier tube (PMT) or an electron-multiplying charge-coupled device (EMCCD) camera. In this work, we mainly use the PMT for state readout. The camera is used when aligning the beams with the ions as done in section 5.2.3.

The diverse electronic components to run the experiments are controlled by a multitude of hardware and software elements. The control software TrICS provides a graphical user interface to edit experimental control parameters such as rf frequencies created by direct digital synthesis (DDS) boards, rf powers to drive acousto-optic modulators (AOM) and voltages for the trap electrodes. The instructions set by the control software are sent to the bus system and the PulseBox [39]. The PulseBox is a field-programmable gate array with multiple, built-in DDS boards. It is the main experimental control hardware and controls the timing of electrical pulses during a sequence, thus controlling the ion-light interactions. The built-in DDS boards allow temporal shaping of the output amplitude and phase-coherent frequency switching. The PulseBox controls the transistor-transistor logic (TTL) pulses that are used to time the laser intensity stabilisation and control electronic rf switches. The bus system controls components that are not switched during an experimental sequence. These include, for example, the power and frequency of DDS sources for the AOMs that do not require phase-coherent switching.

4.2 Raman Beam Setup

For the implementation of the Raman interactions discussed in section 3.2, we create a set of individually controlled beams derived from a single laser source. The Raman beam setup is divided into three parts that can be seen in figure 4.2: the laser source, the AOM setup and the focusing stage. Due to its size, the laser source does not fit on the same optical table as the vacuum chamber and is therefore mounted on a separate optical table. Light from the laser source is sent to the AOM setup, which is mounted on the same optical table as the ion trap, underneath the focusing optics. The AOM setup is used to separate the laser source into three individually controlled beams. These are then guided to the trap to focus them onto the ions.

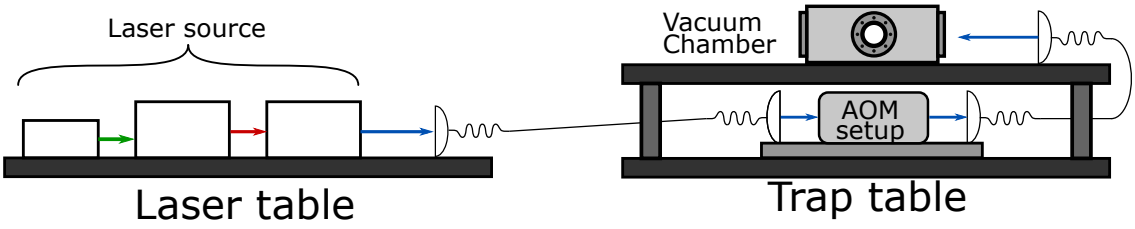

Figure 4.2: Schematic overview of the Raman beam setup. The laser source is mounted on a separate optical table. Via an optical fibre light from the laser source is guided to the trap table, where the AOM setup and the vacuum chamber are mounted. The AOM setup is mounted beneath the vacuum chamber and is used to separate the laser source into three individually controllable beams. The beams are subsequently guided to the vacuum chamber containing the ion trap, where they are focused onto the ions.

4.2.1 Laser source

The laser used to perform operations on the ground state qubit is a continuous wave, frequency-doubled, tunable Ti:Sapphire (Ti:Sa) laser[1]. A schematic setup of the laser source setup is shown in figure 4.3. The light used to pump the Ti:Sapphire is generated by a diode pumped Nd:YAG that is subsequently frequency-doubled to 532 nm[2]. The Ti:Sa is frequency-stabilised via an internal ring resonator. An etalon inside the Ti:Sa's ring resonator allows tuning of outgoing light's wavelength. The outgoing light is frequency-doubled with a lithium triborate (LBO) crystal and frequency-stabilised via a ring resonator. After frequency doubling, the laser provides $\approx 1.2\,\mathrm{W}$ of optical power in the 400 nm region.

The output light of the laser passes a $\lambda/2$-waveplate and a Glan-Laser polariser[3] that allow tuning the power of the transmitted light by rotating the polarisation. As the laser's output beam is elliptical, we use a Galilean beam expander made of two cylindrical lenses with focal lengths $f_1 = -9.7\,\mathrm{mm}$ and $f_2 = 6.35\,\mathrm{mm}$ to expand the beam in the horizontal direction. Afterwards, the light is coupled into a photonic crystal fibre[4] suitable for the operation with high power beams. Coupling the light into the fibre is done via an aspheric singlet fibre collimator[5], as we found these to be suitable for fibre coupling at high powers. When using cemented monochromatic doublets for fibre coupling, we noticed a significant drop in coupling efficiency at high powers. The coupling efficiency would drop from $\approx 60\,\%$ at powers $< 500\,\mathrm{mW}$ to $\approx 30\,\%$ for powers $> 500\,\mathrm{mW}$.

[1] M Squared SolsTiS + ECD-X
[2] Lighthouse Photonics Sprout-G18W
[3] Thorlabs GL10-A
[4] NKT Photonics aeroGUIDE-5-PM
[5] Schäfter+Kirchhoff 60FC-SF-4-A11-01

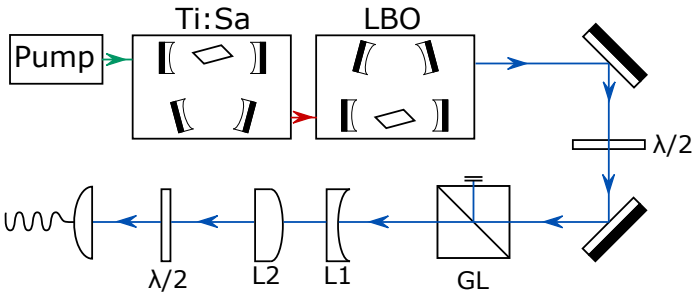

Figure 4.3: Schematic of the laser source. The 532 nm light of a frequency-doubled Nd:YAG pumps the Ti:Sapphire, whose output is subsequently frequency-doubled to 398 nm light via an LBO crystal. The output frequency of the Ti:Sa and the LBO are frequency-stabilised via a ring resonator. A $\lambda/2$-waveplate is used in combination with a Glan-Laser polariser (GL) to tune the power of the transmitted light. Two cylindrical lenses (L1) and (L2) expand the beam in the horizontal direction. Before fiber coupling, the polarisation is rotated to match the slow/fast axis of the fiber.

When performing coherent Raman operations it is important to minimise the photon scattering rate to avoid decoherence [25]. As the scattering rate scales with $\Gamma \propto \Delta^{-2}$ and the Raman Rabi frequency with $\Omega_\mathrm{R} \propto |\Delta|^{-1}$, one can minimise the ratio Γ/Ω_R by increasing the laser detuning with respect to the $4S_{1/2} \leftrightarrow 4P_{1/2}$ transition. The ratio Γ/Ω_R is shown in figure 4.4. Throughout this thesis, we operate the laser at 398.0 nm, 2.4 THz red detuned from the $^{40}\mathrm{Ca}^+$ $4S_{1/2} \leftrightarrow 4P_{1/2}$ transition. We found this to be a suitable compromise between low scattering rates and sufficient ion-light coupling given the available optical power.

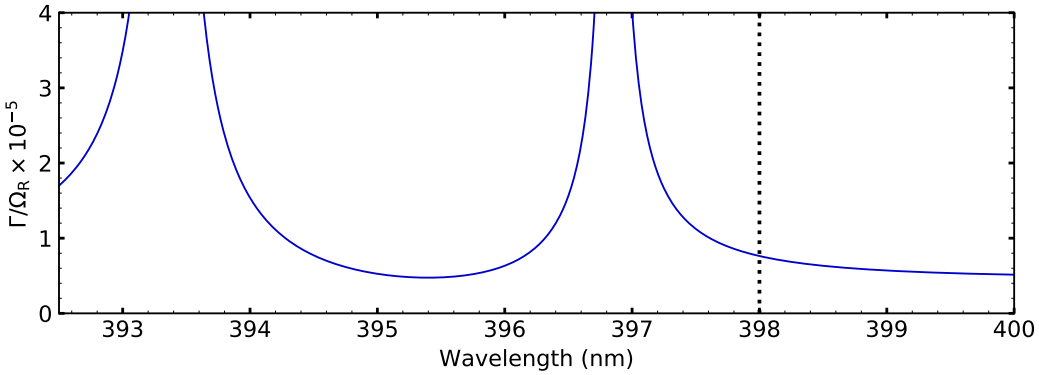

Figure 4.4: Ratio of the total scattering rate Γ to the Raman Rabi frequency Ω_R for different wavelengths. The wavelength of the laser source is set to 398.0 nm (dashed line).

4.2.2 AOM Setup and control

For the implementation of the single- and two-qubit operations discussed in section 3.2 we require Raman beams with different frequencies, from different directions and with different polarisations. A collinear beam pair ($\boldsymbol{\delta k} = 0$), consisting of the beams R_π and $R_\perp$ with orthogonal polarisations, is used to implement motion-insensitive single-qubit operations. The third beam $R_\parallel \perp R_\pi, R_\perp$ is used in combination with either the $R_\perp$ or R_π beam to address the ion's motion for sideband transitions or entangling gate operations. The laser source is divided into the three beams on the AOM setup shown in figure 4.5. Each beam is individually controlled via a separate AOM[6].

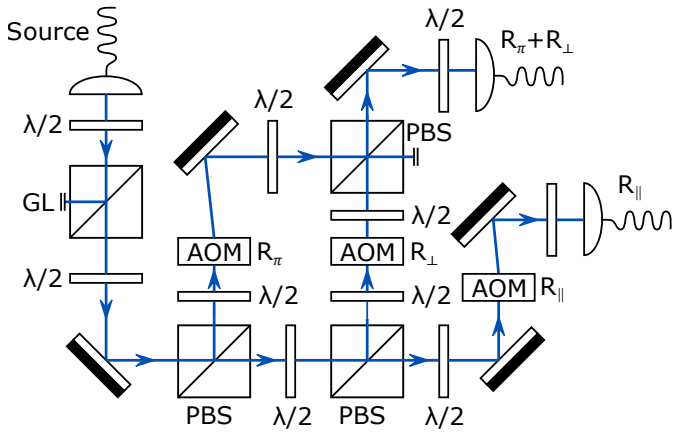

Figure 4.5: Schematic of the AOM switching board. The fibre output is sent through a $\lambda/2$-waveplate and a Glan-laser polariser (GL) to clean the polarisation. The beam is then split into three different branches using polarising beam splitters (PBS). Each beam passes a separately controlled AOM used for switching and frequency shifting. The R_π and $R_\perp$ beam are combined on a PBS and coupled into the same fibre. The $R_\parallel$ beam is coupled into a separate fibre.

First, the output of the fibre is collimated with an air-gapped triplet lens system[7], as we noticed cemented doublet collimators do not withstand optical powers above $\approx 200\,\mathrm{mW}$ at our operating wavelength. After collimation, the beam's polarisation is rotated with a $\lambda/2$-waveplate[8], to maximise the transmission through the following Glan-Laser polariser. The Glan-Laser polariser cleans the polarisation by only transmitting light with a linear polarisation parallel to the table's surface. The beam is then split into three separate paths using polarising beamsplitters[9]

[6] Brimrose QZF-80-40-397
[7] Thorlabs TC06APC-405
[8] Lens Optics W2Z15-397
[9] Thorlabs PBS12-405-HP

(PBS). We set the beam intensity in each branch by setting the polarisation before each PBS with a $\lambda/2$-waveplate.

In each branch there is a separately controlled AOM to control the amplitude and frequency of the beams. Since the AOM's diffraction efficiency is sensitive to the polarisation of the incoming beam, we place a $\lambda/2$-waveplate before each AOM. For each AOM, we only keep the first-order diffracted beam and block the other orders using a pinhole. After passing their respective AOM, the R_π and $R_\perp$ beam are recombined on a PBS and coupled into the same optical fibre. The light of the diffracted $R_\parallel$ beam is coupled into a separate fibre. The fibres are then guided to the vacuum chamber to focus the light onto the ions. Before fibre coupling we use another $\lambda/2$-waveplate to align the beam's polarisation to the fast or slow axis of the fibre.

The radio frequency for each AOM is controlled individually via a series of electronic elements shown in figure 4.6. The rf chain of the $R_\parallel$ beam can be separated into two configurations: The first configuration consists of a single DDS source that generates a monochromatic rf signal. It is used to perform local qubit operations in section 5.2 and 5.4 or the light-shift gate in section 5.3. The second configuration is used for bichromatic modulation of the laser beam, which is used to drive the Raman MS gate described in section 5.4.2. It consists of two separate DDS sources that are operated at different frequencies. The signals of the two DDS sources are combined in a passive power combiner. A radio frequency switch that is controlled via the PulseBox's TTL pulses allows switching between the two configurations.

We noticed that the diffraction angle of the AOMs and therefore the amount of light coupled into the fibres depends on its temperature. In an experimental sequence, this leads to a change in optical power at the ion, as the AOM heats up due to the applied rf. Feeding the AOM with the "idle" signal keeps it at a constant temperature, therefore reducing transient thermal effects when switching the AOMs during a sequence. Following the switch that selects between the monochromatic and bichromatic configuration, an additional switch allows us to forward either the "idle" signal or the selected configuration to the rf amplifier. The "idle" signal is at 115 MHz and is fed to the AOM when the beam is not used. The 115 MHz frequency changes the diffraction angle of the AOM enough that no light leaks through the fibre when it is applied.

The rf chain of the R_π beam is identical to the $R_\parallel$ chain, though without the bichromatic profile. The rf signal for the $R_\perp$ beam's AOM is generated by a PulseBox DDS source that allows for coherent phase control relative to the other DDS. This signal is then amplified with an rf amplifier and fed to the AOM. The output signal of each rf amplifier can be regulated by a voltage-controlled attenuator. This is used in combination with a proportional–integral–derivative (PID) controller to stabilise the beam intensity.

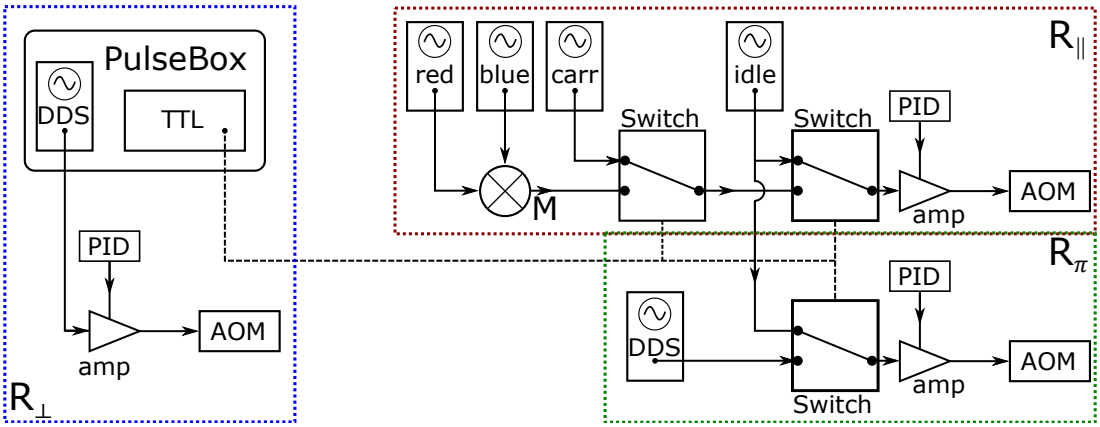

Figure 4.6: Radio frequency chains to control the AOMs. The signal for the $R_\perp$ beam (blue rectangle) is generated by a PulseBox DDS board (DDS) and amplified (amp) before it is fed to the AOM. A controller (PID) feeds back on the rf amplifier's built-in voltage controlled attenuator to stabilise the beam intensity. The PulseBox TTL pulses are used to control electronic switches during sequences. For the $R_\parallel$ beam (red rectangle) either a monochromatic (carr) or bichromatic signal, is applied to the AOM. The bichromatic signal is generated by combining two DDS signals (red) and (blue) in a combiner (M). An "idle" signal (idle) is applied to the AOM to keep it at a constant temperature when it is not turned on. The R_π rf chain (green rectangle) is identical to the R_π rf chain, though without the bichromatic configuration.

4.2.3 Beam geometry at the trap setup

The output light of the two fibres coming from the AOM setup is guided and focused onto the ions, through the slit of the trap chip. A schematic of the geometry and beam path at the trap is shown in figure 4.7.

The R_π and $R_\perp$ form the collinear beam pair. They arrive in the same fibre and are entering the vacuum chamber from a direction orthogonal to the magnetic field. These two beams are polarised orthogonal with respect to each other. The fibre output is collimated to a beam with $\approx 25\,\mathrm{mm}$ diameter. After collimation, $\approx 1\,\%$ of the light is picked off via a beam sampler[10] and focused onto a photodiode to monitor and control the beam intensity.

Depending on the gate mechanism we require different beam polarisations:

- For the light-shift gate performed in section 5.3 the $R_\perp$ and R_π beam are polarised orthogonal and parallel to the magnetic field, respectively. This results in a $\sigma^\pm$ polarisation for the $R_\perp$ beam and a π polarisation for the

[10] Thorlabs BSF10-A

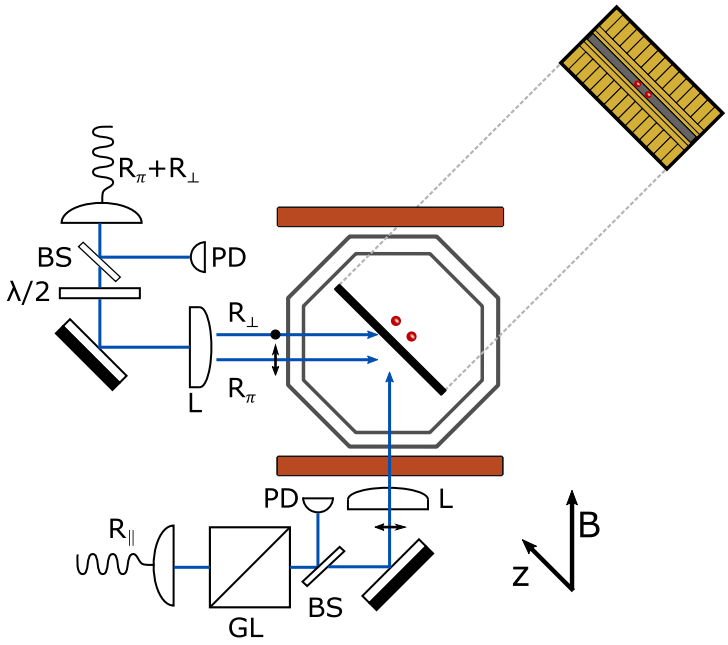

Figure 4.7: Paths of Raman beams to the vacuum chamber. The $R_\perp$ and R_π are guided to the trap via the same fibre, with their polarisation set orthogonal and parallel to the magnetic field (B) via a $\lambda/2$-waveplate. The $R_\parallel$ beam travels along the magnetic field axis. With a Glan-Laser polariser (GL) we set the polarisation parallel to the wavevector of the $R_\perp$ and R_π beam. A $f = 250\,\mathrm{mm}$ lens (L) guides the beams through the slit of the trap and focuses them onto the ions. In this configuration, the differential wave vector vanishes for the parallel beam pair but is aligned with the trap's z-axis for the orthogonal beam pair. In each path light is picked off via a beam sampler (BS) and sent onto a photodiode (PD) for monitoring and intensity stabilisation. The dashed lines are a guide to a view normal to the trap chip surface.

R_π beam. In this configuration the $R_\perp$ and $R_\parallel$ beam do not couple the two ground states with each other.

- When performing the Raman MS gate in section 5.4, we use the $\lambda/2$-waveplate to rotate the $R_\perp$ beam's polarisation to π. With this configuration we can couple the two ground states with the $R_\perp$ and R_π beam. Thus we can use this beam pair to implement single-qubit operations and perform the Raman MS gate.

Therefore, after the beam sampler, we use a $\lambda/2$-waveplate to rotate the polarisation. This allows us to adjust the polarisation depending on the gate mechanism

we are using. The beam is guided onto the ions using a motorised mirror mount[11] and focused with a $f = 250\,\mathrm{mm}$ lens.

The $R_{\parallel}$ beam enters the vacuum chamber parallel to the magnetic field axis. The fibre output is collimated to a beam with $\approx 25\,\mathrm{mm}$ diameter and subsequently passes through a Glan-Laser polariser. This ensures that only light polarised parallel to the table's surface is transmitted. As it travels along the magnetic field with its polarisation orthogonal to the $\sigma_{\pm} = \{1, 0, 1\}$ polarised $R_{\perp}$ beam, we denote its polarisation as $\sigma_{\mp} = \{1, 0, -1\}$. The polarised light is then picked off via a beam sampler and focused onto a photodiode for intensity stabilisation. After the pick-off, the beam is focused onto the ions using a $f = 250\,\mathrm{mm}$ lens. In this configuration the difference wave vector of the orthogonal beam pair, i.e. the $R_{\perp}$ and $R_{\parallel}$ beam, lies along the axial direction of the trap. This allows us to address the ions' axial motional modes, which is required for the entangling gates and operations on the motional sidebands. Since the difference wave vector does not overlap with the radial direction, this configuration is also insensitive to the radial motion.

The intensity stabilisation is implemented by measuring the power on the photodiode and feeding back on the rf power of the AOM. Via the photodiode, we measure the optical power as a voltage. The target voltage, and thus the desired beam intensity, can be set via the experiment computer. We feed the photodiode voltage and setpoint to an analogue sample-and-hold PID controller which creates the control signal. At the beginning of each sequence, we turn on the beams for 3 ms and measure their intensity on the photodiode. During this sampling time, the PID controller creates the control signal and feeds it to the rf amplifier's built-in voltage-controlled attenuator. This changes the rf power fed to the AOM, thus controlling the optical power. The beams are then turned off and a TTL pulse switches the PID controller to hold the last value of the control signal throughout the sequence, until a new value is sampled.

[11] Newport Motorized Mirror Mount 8821

5 Qubit operations

In this chapter, we present single- and two-qubit operations on the ground state qubit of $^{40}Ca^{+}$ ions using Raman interactions. In section 5.2.1 we show Raman spectroscopy on two ions to determine the frequencies of the carrier transition and the motional sidebands of the axial motion. Next, in section 5.2.2 we use Ramsey and spin-echo measurements to determine the coherence time of our setup. In section 5.2.3 we discuss the stability and benchmark the performance of our setup.

In section 5.3 and 5.4 we generate entanglement between two ions using the geometric phase gate and the Raman MS gate. We discuss how we calibrate the gate interactions to create an entangling gate. Finally, we evaluate the fidelity for each method.

5.1 State preparation and readout

Before performing coherent qubit operations, we need to initialize the ions. First, the ions are optically pumped for $\approx 800\,\mu s$ to the state $|\downarrow\rangle$. This is done by transferring the state population from $|\uparrow\rangle$ to the state $|3D_{5/2}, m_j = -5/2\rangle$ using the 729 nm laser. The ions are simultaneously excited to the state $|4P_{3/2}, m_j = -3/2\rangle$ using the 854 nm laser. From this state the ions decay with 96 % probability to the $4S_{1/2}$-manifold. In 4 % of the cases the ions decay to the $3D_{3/2}$-manifold, in which case they are transferred to the $4P_{3/2}$-manifold with an 866 nm laser resonant with the $3D_{3/2} \leftrightarrow 4P_{3/2}$ transition. Due to the dipole selection rules, starting from the state $|4P_{3/2}, m_j = -3/2\rangle$ the only accessible state through spontaneous decay to the $4S_{1/2}$-manifold is the state $|\downarrow\rangle$.

We quantify the residual population in the undesired state $|\uparrow\rangle$ after optical pumping, by shelving it to the $3D_{5/2}$ level via a resonant π-pulse with the 729 nm laser. The ions are then illuminated with 397 nm light for fluorescence detection. If the ions were previously in the state $|\uparrow\rangle$, we observe no fluorescence. By averaging over 6200 shots we find the state preparation error $\epsilon_p = 2.6(6) \times 10^{-3}$. Note that this value only represents an upper bound of the state preparation error, as it also includes errors due to imperfect shelving of the state $|\uparrow\rangle$ to the $3D_{5/2}$ level.

After optical pumping, we do 5 cycles of sideband cooling with the 729 nm laser, each consisting of cooling the axial centre of mass mode for $\approx 1\,ms$ and the axial breathing mode for $\approx 500\,\mu s$. As the ions decay faster to the ground state from the $4P_{3/2}$-manifold than the $3D_{5/2}$-manifold, we simultaneously illuminate the ions with the 854 nm laser to transfer them to the $|4P_{3/2}, m_j = -3/2\rangle$ state. The cycle is completed with another stage of optical pumping to ensure that the ions are in the state $|\downarrow\rangle$. After repeating this cycle for 5 times, we achieve a residual mean phonon number $\bar{n} \approx 0.05(2)$.

For measuring the ion's final state, we apply a π-pulse with the 729 nm beam

to shelve the population from $|\downarrow\rangle$ to the $3D_{5/2}$ level. Afterwards, the ions are continuously illuminated with 397 nm light red detuned from the $4S_{1/2} \leftrightarrow 4P_{1/2}$ transition. During this time, we measure the fluorescence light on the PMT and determine the state via the photon count rate histograms. If the ion was in the state $|\downarrow\rangle$, the shelving pulse transfers it to the $3D_{5/2}$ level. In this state the ion appears dark, i.e. no fluorescence is observed. If the ion is not shelved we observe fluorescence light, which increases the photon count rate. For two ions the photon count rate is doubled if both ions emit fluorescence light. For a readout time of 5 ms the photon count rate histograms for two dark ions, one dark ion and zero dark ions are well separated and the threshold for each case can be set manually.

We determine the shelving error ϵ_{r} by comparing the unsuccessful shelving events with the successful shelving events. We define the shelving as successful if the ions appear dark after shelving. By averaging over 3150 shots, we find the ratio between unsuccessful shelving pulses and successful shelving pulses to be $\epsilon_{\mathrm{r}} = 9(2) \times 10^{-3}$. We suspect that this is caused by laser intensity noise and state preparation and measurement errors.

5.2 Single-qubit Raman operations

5.2.1 Raman spectroscopy

An essential ingredient for quantum information processing is being able to coherently transfer populations between the $|\downarrow\rangle$ and $|\uparrow\rangle$ state. For this we first need to determine the frequency difference between the two ground states. This is done by performing spectroscopy on two ions with the $\mathrm{R}_{\parallel}$ and the $\mathrm{R}_{\perp}$ beams of the orthogonal beam pair, as in this configuration we are also able to observe the sidebands of the axial motion. By keeping the $\mathrm{R}_{\perp}$ beam's frequency constant, and varying the frequency of the $\mathrm{R}_{\parallel}$ beam, we are able to tune the resulting beat note's frequency that the ions experience. If the beat frequency matches the ions' transition frequencies, we are able to transfer the population between states. As the ions are initialised in $|\downarrow\downarrow\rangle$, we would observe this as a peak of the excitation defined as $p_{\uparrow\uparrow} + (p_{\downarrow\uparrow} + p_{\uparrow\downarrow})/2$, where $p_{\uparrow\uparrow}$ and $p_{\downarrow\uparrow} + p_{\uparrow\downarrow}$ denote the likelihood of measuring the ions in the state $|\uparrow\uparrow\rangle$ and $|\downarrow\uparrow\rangle$ or $|\uparrow\downarrow\rangle$, respectively.

The results of the Raman spectroscopy on two ions is shown in figure 5.1. We identify three clear peaks in the spectrum. In ascending order of the frequency, these correspond to the carrier transition and blue sideband transitions of the axial COM mode and breathing mode respectively. Note that we only consider the blue sidebands, as the ions are cooled close to their motional ground states in which case the red sidebands cannot be observed.

We determine the transition frequencies by fitting a Lorentzian lineshape to our data. It should be noted that a complete description of the spectrum would re-

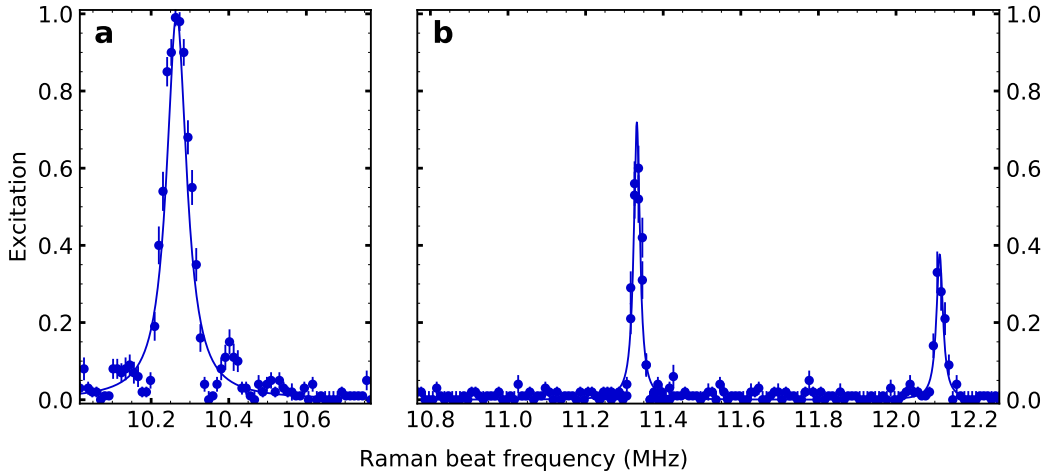

Figure 5.1: Raman spectroscopy on two ions with the $R_\perp$ and $R_\parallel$ beam with (a) 10 µs and (b) 30 µs probe time. In ascending order of the frequency the dips show the carrier transition, the blue sideband transition of the axial COM mode and the blue sideband transition of the axial breathing mode. Solid blue lines show Lorentzian fits to determine the frequencies of the dips.

quire a fit to equation 3.8. A Lorentzian fit finds the centre frequency equally well due to the symmetry of the lineshape but has the advantage that it requires fewer free parameters, thus making the fit more robust. At $\delta_c = 10.267(2)$ MHz we observe the carrier transition between $|\downarrow\downarrow\rangle$ and $|\uparrow\uparrow\rangle$. With a ground state splitting of 2.802 41 MHz/G this corresponds to a magnetic field of 3.6636(7) G. The blue sideband of the COM mode is visible at $\delta_{com} = 11.3321(5)$ MHz and the one of the breathing mode is visible at 12.1116(7) MHz. The errors represent the uncertainties determined by the fit. From this, we are able to extract $\omega_z = \delta_{com} - \delta_c = 2\pi \times 1.065(2)$ MHz.

In order to observe Rabi oscillations and transfer the state population, we apply Raman pulses with the beat frequency resonant with the carrier transition. The results are shown in figure 5.2. We observe Rabi oscillations as predicted in equation 3.8. At 10 µs the population is completely transferred from the $|\downarrow\downarrow\rangle$ to the $|\uparrow\uparrow\rangle$ state, as indicated by the excitation reaching 1. We find the Rabi frequency $\Omega = 2\pi \times 49.55(7)$ kHz by fitting equation 3.8 with $\Delta = 0$ to the data via a least-squares fit.

5.2.2 Ramsey & spin-echo coherence measurements

As our ions are not a perfectly isolated system but are subject to environmental noise such as magnetic field noise or relative laser phase fluctuation, the timescale on which we can reliably perform gate operations is limited by decoherence induced

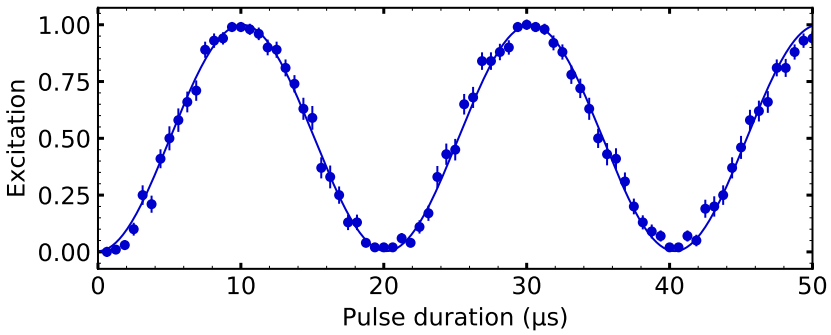

Figure 5.2: Rabi oscillations on the carrier transition of the ground state qubit. Solid lines shows a fit to eq. 3.8 to determine the Rabi frequency $\Omega = 2\pi \times 49.55(7)\,\mathrm{kHz}$.

by the environment. We use Ramsey and spin-echo sequences introduced in section 3.3 to quantify the coherence time of our ground state qubit.

We perform Ramsey and spin-echo measurements with the $R_\perp$ and $R_\parallel$ beam pair on two ions, as this beam pair is also used to entangle two ions. First, we apply a carrier $\pi/2$-pulse that transfers the $|\downarrow\downarrow\rangle$ state to a superposition $(|\downarrow\downarrow\rangle + |\uparrow\downarrow\rangle + |\downarrow\uparrow\rangle + |\uparrow\uparrow\rangle)/2$. The lasers are then turned off for a wait time τ_R, during which the qubit state acquires a phase $\Phi \propto \tau_\mathrm{R}$. After the wait time we apply a second carrier $\pi/2$-pulse with varying phase ϕ. Ideally, this results in full contrast oscillations of the excitation as a function of ϕ as described in equation 3.9. However, through decoherence the contrast is lowered.

For our setup, we expect magnetic field noise and relative laser phase noise to be the dominant sources of decoherence. The former is expected due to the ground state's relatively high magnetic field sensitivity compared to the optical qubit. The latter is expected, as we are performing the Ramsey experiment with two orthogonal beams. Thus, noise in the optical path of either beam will lead to noise in the relative laser phase.

We insert a carrier π-pulse at a time $\tau_\mathrm{R}/2$ after the first Ramsey $\pi/2$-pulse to create a spin-echo sequence. The second Ramsey $\pi/2$-pulse is applied at a time $\tau_\mathrm{R}/2$ after the π-pulse. The π-pulse transfers the populations from $|\downarrow\downarrow\rangle$ to $|\uparrow\uparrow\rangle$ and from $|\uparrow\downarrow\rangle$ to $|\downarrow\uparrow\rangle$, and vice versa. This cancels the acquired phase if the magnetic field does not change in the second half. However, if the magnetic field noise is fast compared to $t_\mathrm{R}/2$, the acquired phase is different in each half and will not be compensated. Unlike slow magnetic field fluctuations, phase noise cannot be cancelled by using a spin-echo sequence.

Figure 5.3 shows the results for Ramsey and spin-echo measurements for wait times $\tau_\mathrm{R} = 0\,\mathrm{ms}$ and $\tau_\mathrm{R} = 5\,\mathrm{ms}$. As expected, the excitation shows oscillations depending on the phase of the final $\pi/2$-pulse. For a wait time $\tau_\mathrm{R} = 0\,\mathrm{ms}$ the

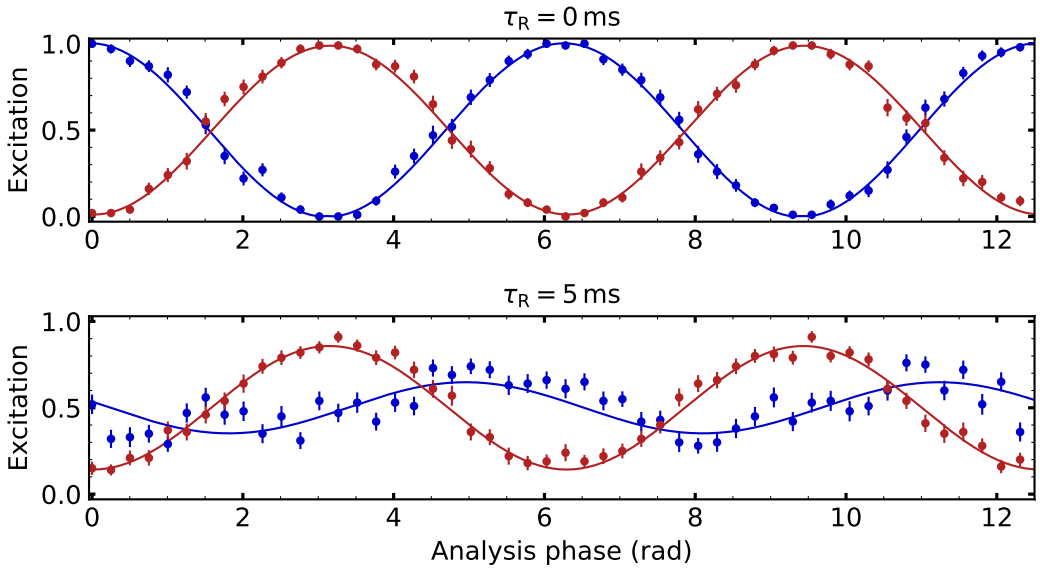

Figure 5.3: Ramsey (blue) and spin-echo (red) measurements on two ions. Solid lines show sinusoidal fits to determine the contrast.

contrast of the oscillations is close to unity for both sequences. Moreover, the two curves are out of phase by $\approx \pi$, which is expected as for the Ramsey sequence the state is rotated for 2π, whereas for the spin-echo sequence the state is rotated by π. For a wait time $\tau_R = 5\,\text{ms}$ we observe that the contrast has dropped significantly to 0.30(2) and 0.72(2) for the Ramsey and spin-echo sequence, respectively.

We now determine the coherence time τ_c for the Ramsey and spin-echo method. For this, we evaluate the contrast of the oscillations for different wait times τ_R by fitting the data to sinusoidal oscillation and extracting the contrast C. The results are shown in figure 5.4. The figure demonstrates that the decay in contrast is slower for the spin-echo sequence than for the Ramsey sequence. Moreover, we notice that the shape of the decay curve is similar to a Gaussian function. By fitting a Gaussian curve $C = A\exp(\tau_R^2/\tau_c^2)$ to our data we find the coherence times $\tau_{c,\text{Ramsey}} = 4.66(7)\,\text{ms}$ and $\tau_{c,\text{echo}} = 9.7(1)\,\text{ms}$ for the Ramsey and spin-echo sequence, respectively. The initial contrast A accounts for state preparation and measurement (SPAM) errors.

We compare the Ramsey and spin-echo measurements with measurements previously performed on the ground state qubit with the 729 nm laser to determine the cause of decoherence. With the 729 nm laser, a decay constant of $\tau_{c,729} \approx 80\,\text{ms}$ has been measured in a spin-echo experiment. Since this is significantly larger than $\tau_{c,\text{echo}} = 9.7(1)\,\text{ms}$, we suspect that the dominant source of decoherence is caused by instabilities of the relative phase between the Raman beam pair. We suspect that the phase instabilities are caused by noise in the beams' optical paths, which

could be caused by mechanical vibrations of the optical setup.

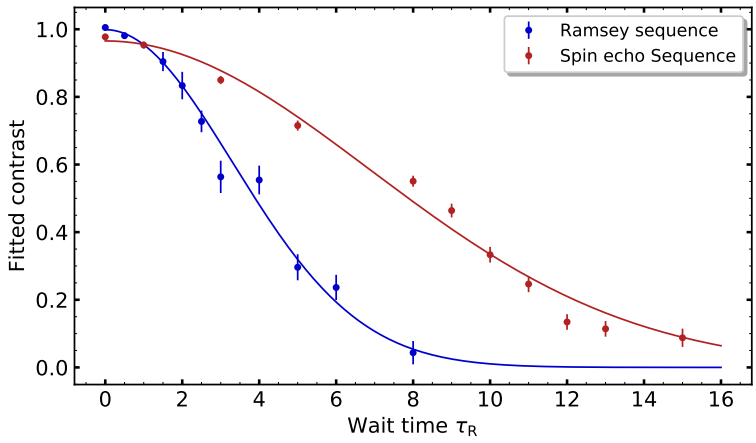

Figure 5.4: Coherence time of two ions measured with the $R_\perp$ and $R_\parallel$ beam. The Gaussian fits yield coherence times $\tau_{c,\mathrm{Ramsey}} = 4.66(7)\,\mathrm{ms}$ and $\tau_{c,\mathrm{echo}} = 9.7(1)\,\mathrm{ms}$ for the Ramsey and spin-echo sequence respectively.

5.2.3 Error analysis

The pulse duration necessary to carry out single- and two-qubit operations depends on the Rabi frequency. Since the Rabi frequency depends on the beam intensity at the ion, variations in intensity will change the pulse duration required for qubit operations. If these changes occur during an experimental trial, subsequent gate pulses result in either over- or under-rotation of the qubit state, leading to errors in the gate sequence. Thus short-term intensity stability on the timescale of an experimental trial is important to mitigate this error. Rabi frequency drifts that are slow compared to experimental trials might not affect the quality of a single experimental trial, but require time-consuming re-calibration of the gate duration. Moreover, when performing identical single-qubit gates on two ions simultaneously, we require identical Rabi frequencies for the two ions. This can be achieved by illuminating the ions equally. We use Rabi oscillations to analyse the effects of beam alignment on the short-term intensity fluctuations and the long-term stability of the Rabi frequency. By comparing Rabi oscillations on two ions simultaneously, we determine their Rabi frequencies and align the beams to equalise them.

Effects of beam alignment

Since the spatial intensity distribution of the focused Raman beam is not described by a plane wave, but a Gaussian beam profile, the electric field experienced by the ion depends on the ion's position relative to the beam. Changes in beam position

relative to the ion, caused by slow thermal drifts or vibrations of the trap setup relative to the optics, lead to changes in the Rabi frequency. At the beam focus, the radial intensity distribution follows a Gaussian curve, with its maximum at the centre. As the minimum intensity gradient is at the beam centre, centring the beam around the ion reduces the sensitivity to beam pointing noise.

We centre the beam on a single ion by maximising the Rabi frequency. First, the ion is initialised the state $|\downarrow\rangle$. Next, we induce Rabi oscillations and set the pulse duration to a point where the populations of the states $|\downarrow\rangle$ and $|\uparrow\rangle$ are equalised. At this point the populations are the most sensitive to changes in Rabi frequency. We steer the mirror to maximise population in the $|\uparrow\rangle$ state, as this indicates an increase of the Rabi frequency. We perform this method on higher-order fringes of the Rabi oscillation to increase the sensitivity to beam alignment.

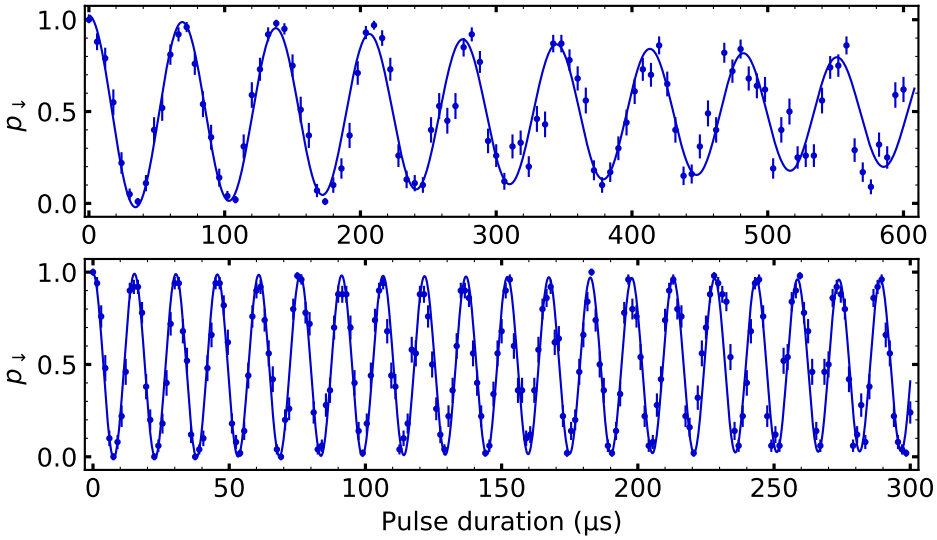

Figure 5.5: Rabi oscillations driven by a with non-optimised (top) and optimised (bottom) beam alignment. Beam alignment is optimised by centring the beam on the ion, which maximises the Rabi frequency. The solid line shows a fit to a Rabi oscillation with decay according to equation 5.1. We find $\Omega = 2\pi \times 14.52(1)\,\mathrm{kHz}$ and $\alpha = 14(1)$ for the non-optimised alignment and $\Omega = 2\pi \times 65.74(1)\,\mathrm{kHz}$ and $\alpha = 257(43)$ for the optimised alignment.

A comparison of Rabi flops with non-optimised and optimised beam pointing is shown in figure 5.5[12]. We usually find the beams in the non-optimised alignment

[12]We notice that in both cases $p_\downarrow < 1$ even if no pulse is applied. This is not expected since the ion is initialised in the $|\downarrow\rangle$ state. In this case the laser frequency of the shelving pulse drifted off-resonance. Hence, the state $|\downarrow\rangle$ is not fully transferred to the $3D_{5/2}$ level, which reduces the accuracy to measure the ion's state as $|\downarrow\rangle$.

after a couple of days of not realigning them. Optimising the beam alignment by maximising the Rabi frequency increases the Rabi frequency by a factor of 4.5 compared to the original alignment. For the non-optimised alignment we observe a decay in contrast after 8 periods, whereas for the optimised case, even after 19 periods, we do not observe any significant decay. We fit our data to the model

$$p_{\downarrow} = \frac{a + b\cos(\Omega t)e^{-t\Omega/(2\pi\alpha)}}{2}, \tag{5.1}$$

to determine the Rabi frequency Ω and the relative decay constant α. The factors a and b include the readout error due to the off-resonant shelving pulse. The model recovers resonant Rabi oscillations from equation 3.8 for parameters $\alpha = \infty$ and $a = b = 1$. For the non-optimised beam alignment we find $\Omega = 2\pi \times 14.52(1)\,\mathrm{kHz}$ and $\alpha = 14(1)$. For the optimised beam alignment we find $\Omega = 2\pi \times 65.74(1)\,\mathrm{kHz}$ and $\alpha = 257(43)$. The relative decay constant α can be seen as a measure of stability, as it expresses how many Rabi oscillations can be performed before the contrast drops to $1/e$. Comparing the two cases, we find that centering the beam on the ion by maximising the Rabi frequency increases α by a factor of 18(3).

Long-term stability

We measure the long-term stability of the Rabi frequency by monitoring the population after a Rabi oscillation. The population is most sensitive to Rabi frequency fluctuations when $p_{\downarrow} = p_{\uparrow} = 0.5$, at $\Omega t = (2n+1)\pi/2$, with n denoting a positive integer. Since the sensitivity increases with n, we choose to monitor the populations at $\Omega t = 18.5\pi$. The data is recorded over 70 min with 200 shots per data point. The results shown in figure 5.6 exhibit a periodic modulation of the excitation probability with a period of $T = 33.3(1)\,\mathrm{min}$. This modulation is synchronous with the temperature drifts in the laboratory caused by the air-conditioning cycle. We suspect that the change in temperature leads to polarisation drifts through the optical fibre that carries the $R_{\perp}$ beam, leading to drifts in the Rabi frequency. We fit Rabi oscillations from equation 3.8 with $\Delta = 0$ and time-dependent Rabi frequency

$$\Omega(t) = \Omega_0(1 + \epsilon_{\Omega}\cos(2\pi t/T)), \tag{5.2}$$

with Ω_0 denoting the Rabi frequency at the start of the measurement, T the oscillation period and ϵ_{Ω} the relative amplitude of the fluctuation. From this we extract that the Rabi frequency oscillates around the ideal value with an amplitude of $\epsilon_{\Omega} = 5.72(6) \times 10^{-3}$. If the duration of the π-pulse was calibrated at a maximum of the Rabi frequency to obtain $p_{\uparrow} = 1$, after 8.32(2) min the same pulse duration would over- or under-rotate the state by $1.005\,72(6)\,\Omega t$. For a π-pulse, this would cause an error that is on the same order of magnitude as the SPAM error.

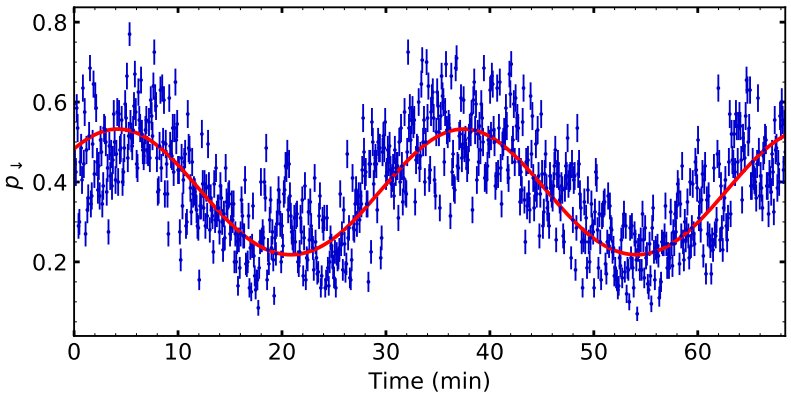

Figure 5.6: Long term stability measurement of $p_\downarrow$ after a Rabi oscillation with the pulse duration initially set to $\Omega t = 18.5\pi$. Each data point consists of 200 repetitions. The solid red line models the Rabi oscillations with a time dependent Rabi frequency described in equation 5.2 with period $T = 33.28(1)$ min and relative amplitude $\epsilon_\Omega = 5.72(6) \times 10^{-3}$.

Unequal illumination

When performing local operations on two qubits simultaneously, it is crucial that they are illuminated equally by the laser, such that their Rabi frequencies are identical. If the two ions have different Rabi frequencies, performing simultaneous Rabi oscillations would result in one ion's state being over- or under-rotated with respect to the other ion, therefore lowering the fidelity of the global qubit rotation.

In order to determine the ions' respective Rabi frequency, we drive Rabi oscillations and monitor the state evolution. Since the PMT detection does not allow us to detect the state of each ion individually, we perform this measurement with the EMCCD camera. Figure 5.7 shows the two ion Rabi oscillations. Here, the Rabi oscillations are driven by the collinear beam pair. For unequally illuminated ions, the phase difference between the two Rabi oscillations is already visible after a 2π-pulse. By fitting the data to equation 3.8 we find the Rabi frequencies $\Omega_1^{\mathrm{u}} = 2\pi \times 46.93(5)\,\mathrm{kHz}$ and $\Omega_2^{\mathrm{u}} = 2\pi \times 50.01(5)\,\mathrm{kHz}$ for the first and the second ion respectively. This leads to a significant error in the populations, as after a 2π oscillations of the first ion, only 96.2 % of the second ion would be reverted to the initial state.

We balance the illumination of the two ions by equalising the Rabi frequency of the two ions by adjusting the beam alignment. This is done by tuning the horizontal axis of the motorised mirror mount. The state evolution of the two ions with balanced illumination is shown in figure 5.7. By fitting eq. 3.8 to the data we find the Rabi frequencies $\Omega_1^{\mathrm{e}} = 2\pi \times 49.83(6)\,\mathrm{kHz}$ and $\Omega_2^{\mathrm{e}} = 2\pi \times 49.48(6)\,\mathrm{kHz}$.

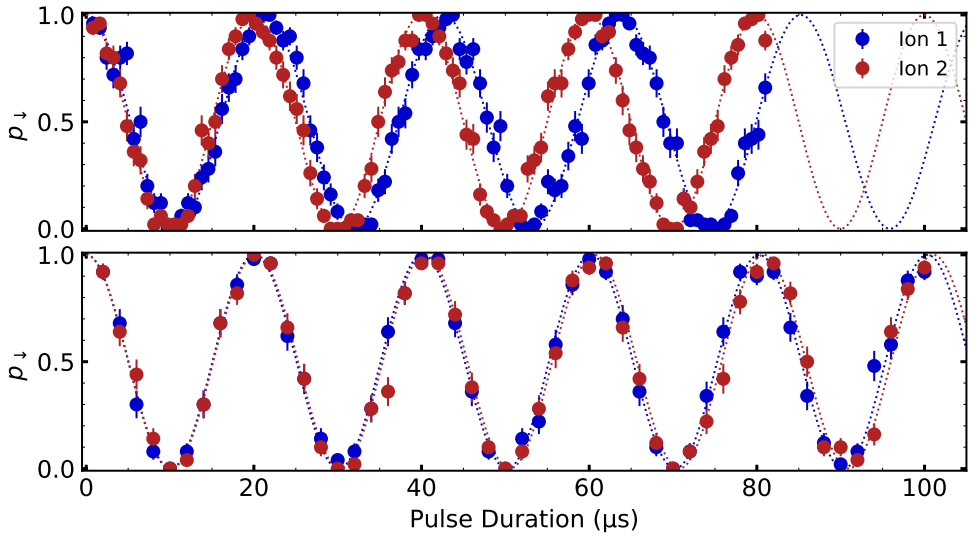

Figure 5.7: Simultaneous Rabi oscillations of two unequally (top) and equally (bottom) illuminated ions. Unequal Rabi frequencies caused by unequally illuminated ions leads to a phase difference between the two ions' state evolution. By properly aligning the beam on the two ions, their Rabi frequencies are approximately equalised. The dashed lines show fits to determine the Rabi frequencies.

5.3 Light-shift gate

In this section we present the implementation of the light-shift gate discussed in section 3.3.1. We demonstrate how we set the ion spacing for an efficient gate performance. We perform the gate within a Ramsey and spin-echo sequence to entangle two ions and determine the gate performance.

5.3.1 Calibrating the ion spacing

The first step in setting up the light-shift gate is setting the ion spacing to optimise the gate efficiency as discussed in section 3.3.1. This lowers the required beam power for any given gate time. In order to maximise the gate efficiency, the relative phase ϕ_z of the light-shift that the ions experience has to be either 2π or π, such that only the states $|\downarrow\downarrow\rangle$ and $|\uparrow\uparrow\rangle$ or $|\downarrow\uparrow\rangle$ and $|\uparrow\downarrow\rangle$ experience a force. As described in equation 3.31, this phase is determined by the ions' position relative to the standing wave pattern created by the $R_\perp$ and $R_\parallel$ beam. Thus, the spacing Δz should be set to either exactly a multiple integer or half-integer of the standing wave pattern's wavelength λ_{sw}, i.e. $\Delta z = 2n\lambda_{\mathrm{sw}}$ or $\Delta z = (n + 1/2)\lambda_{\mathrm{sw}}$, with positive integer n.

For the spacing $\Delta z = (n+1/2)\lambda_{\mathrm{sw}}$, we find $\phi_z = (2n+1)\pi$. In this configuration, performing the gate on the axial COM mode does not create a net force on the

states $|\uparrow\uparrow\rangle$ and $|\downarrow\downarrow\rangle$, but only the states $|\uparrow\downarrow\rangle$ and $|\downarrow\uparrow\rangle$ as can be seen in equations 3.32-3.35. Hence, the motion is only excited if the ions are in the state $|\uparrow\downarrow\rangle$ or $|\downarrow\uparrow\rangle$. Therefore, only these states will acquire a geometric phase. If the spacing is not exactly a half-integer multiple of λ_{sw}, and $\pi/2 < \phi_z < 3\pi/2$, the gate operation also creates a force on the states $|\uparrow\uparrow\rangle$ and $|\downarrow\downarrow\rangle$, albeit with a weaker amplitude. As the force is weaker, the area enclosed in the motional loop is smaller for the states $|\uparrow\uparrow\rangle$ and $|\downarrow\downarrow\rangle$, thus they acquire a geometric phase $\Phi_{\mathrm{even}} < \Phi_{\mathrm{odd}}$. We obtain the propagator $U_{\mathrm{phase}} = \mathrm{diag}(1, i, i, 1)$ from equation 3.39, if $\Phi = \Phi_{\mathrm{odd}} - \Phi_{\mathrm{even}} = \pi/2$. For a given gate duration, Φ is determined by the light-shift amplitude and can be set via the beam power. Therefore, if the spacing is not exactly half-integer multiple, the total qubit state acquires an additional global phase, which increases the required beam power to obtain U_{phase}.

Since the distance between the ions depends on the axial trap frequency, we can change it by adjusting the axial confinement by changing the static voltages on the trap electrodes. In this thesis we set the ion spacing to a half-integer value of the standing wave pattern, although one could in principle use integer spacing. Similar to the Lamb-Dicke factor from equation 3.25, the standing wave pattern experienced by the ion is proportional to the beams' difference wavevector projected onto the axial trap direction. Hence, by determining the Lamb-Dicke parameter, we are able to extract the beam geometry. Comparing the ideal Lamb-Dicke factor η_{ideal} for a beam pair at a 90° angle with the measured Lamb-Dicke factor, we find $\xi = \eta_{\mathrm{measured}}/\eta_{\mathrm{ideal}} = 0.987(3)$. This could be explained by the beams being at a $90° - 1.5(3)°$ angle. From this we determine the wavelength of the standing wave pattern the ions experience by $\lambda_{\mathrm{sw}} = \lambda/(\sqrt{2}\xi)$, where $\lambda = 398.0\,\mathrm{nm}$ is the laser's wavelength. We set the frequency of the axial COM mode to $\omega_z = 2\pi \times 1.093\,\mathrm{MHz}$. According to equation 2.17 this leads to an ion spacing $\Delta z = 5.270\,\mu\mathrm{m} \approx 18.5\,\lambda_{\mathrm{sw}}$. With our setup we are able to control the inter-ion distance with a precision on the order of $\approx 100\,\mathrm{pm}$.

We calibrate the ion spacing by setting the frequency difference between the $\mathrm{R}_\perp$ and $\mathrm{R}_\parallel$ beam to be resonant either with the COM mode or the breathing mode. With the spacing set to a half-integer multiple of the standing wave pattern, we expect to observe only excitation of the axial breathing mode. Applying a pulse with this beam pair then creates a coherent motional state of the corresponding mode with an amplitude proportional to the light-shift force. However, it does not change the population of the ions' electronic states. We read out the motional excitation by probing the $|4S_{1/2}, m_j = -1/2\rangle \leftrightarrow |3D_{5/2}, m_j = -1/2\rangle$ transition with a π-pulse on the respective red sideband. If there is motional excitation in the respective mode, the electron is shelved to the $|3D_{5/2}\rangle$ state and we observe no fluorescence. We vary the ion spacing through the axial confinement until we find a minimum of the COM mode excitation.

The results for the ion spacing calibration measurement are shown in figure

5.8. With p_{dd} and p_{db} denoting the likelihood of measuring both ions and one ion dark, respectively, we define the shelved population as $1 - p_{\mathrm{dd}} - 0.5p_{\mathrm{db}}$. When resonantly exciting the axial COM mode with the Raman beam pair, we mostly observe $< 10\,\%$ of the population being shelved to the $|3D_{5/2}\rangle$ state, even after 2 ms. Though for the breathing mode we observe shelving to the $|3D_{5/2}\rangle$ state with $\approx 40\,\%$ after 30 µs of exciting the mode with the Raman beam pair. We continue our measurements with $\omega_z = 1.093$ MHz, as we are not able to reduce the excitation of the COM mode with different settings of ω_z. We suspect that this is caused by the unequal illumination of the ions.

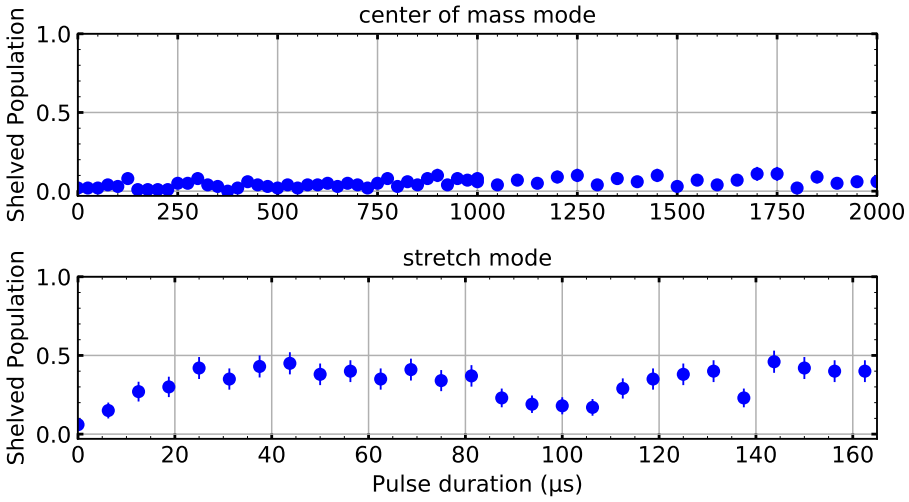

Figure 5.8: Motional excitation of the axial centre of mass mode (top) and the stretch mode (bottom) for two ions after application of the light-shift gate. If the respective motional mode is excited, the electronic state is shelved to the state $|3D_{5/2}, m_j = -1/2\rangle$ via a π-pulse on the red sideband. The ion spacing is set to $18.5\,\lambda_{\mathrm{sw}}$.

5.3.2 Setting up the gate

After calibrating the ion spacing, we calibrate the laser power and detuning for the entangling gate operation. For this, we apply the gate sequence shown in figure 5.9(a). In this sequence, the $\pi/2$-pulses are performed with the collinear beam pair, whereas the gate pulse $g(t)$ is performed with the $\mathrm{R}_{\perp}$ and $\mathrm{R}_{\parallel}$ beam. We calibrate the gate as follows:

1. The $\pi/2$-pulses are calibrated by driving Rabi oscillations and determining the Rabi frequency via a fit as done in section 5.2. After calibrating the $\pi/2$ pulses, the powers and the detuning of the $\mathrm{R}_{\perp}$ and R_{π} beam are held constant.

2. We choose the desired gate time $t_g = 2\pi/\delta_g$ and set the frequency of the $R_\parallel$ beam relative to the $R_\perp$ beam to $\omega_z + \delta_g$. The power of the $R_\parallel$ beam is set approximately to the expected value given by equation 3.38.

3. We execute the gate sequence for different lengths of the gate pulse, and tune t_g to the value where $p_{\uparrow\downarrow} + p_{\downarrow\uparrow}$ minimised, as this indicates that the loops in phase space are closed.

4. We then adjust the power of the $R_\parallel$ beam to a value, where $p_{\uparrow\uparrow}$ and $p_{\downarrow\downarrow}$ are equalised.

5. If there is residual excitation of the states $|\downarrow\uparrow\rangle$ or $|\uparrow\downarrow\rangle$, we minimise it by setting the phase of the second $\pi/2$-pulse. This is done to compensate for single-qubit phases acquired during the sequence. Though we found that this last step is not necessary when the gate is performed within a spin-echo sequence as done in section 5.3.4, since single-qubit phases are already compensated within an echo sequence.

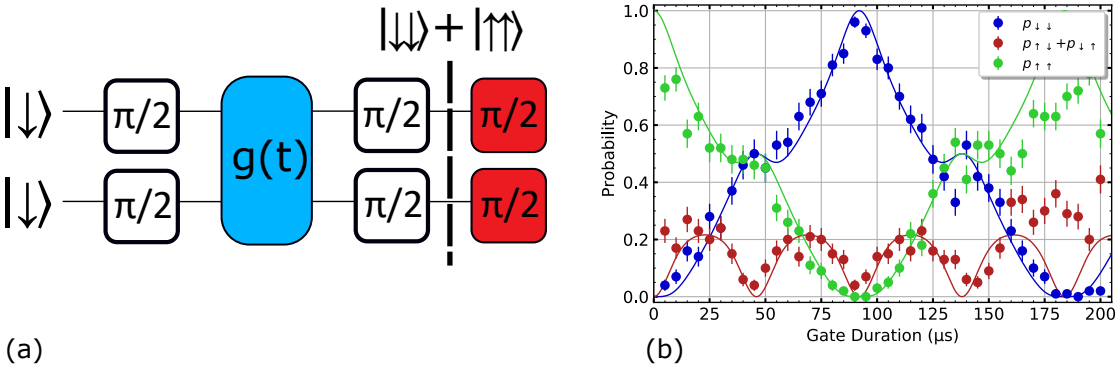

Figure 5.9: Entangling gate with the phase gate embedded in a Ramsey sequence. The sequence (a) starts by applying a $\pi/2$-pulse on both ions simultaneously, followed by the phase gate interaction $g(t)$. For $t = t_g$ the second $\pi/2$-pulse rotates the ions into the Bell state Φ^+. After the Bell state is created, applying another $\pi/2$-pulse and scanning its phase results in parity oscillation that are used to determine the state fidelity. In (b) the state evolution for different durations t of the gate pulse $g(t)$ is shown. Solid lines show solutions of equation 3.31 for an ideal 45 µs gate. Dips in $p_{\downarrow\uparrow} + p_{\uparrow\downarrow}$ indicate that the loops in phase space are closed.

The resulting population dynamics for a calibrated 45 µs phase gate are shown in figure 5.9(b) together with the theoretical prediction from equation 3.31. For the theoretical prediction we assume an ideal gate such that the geometric phase $\Phi = \pi/2$ for $t = t_g$. We see that after creating an entangled state at 45 µs, the ions

are repeatedly disentangled and entangled. At $2t_g$ the population is almost fully transferred to the $|\downarrow\downarrow\rangle$ state, which shows that the ions are disentangled. At this point, the second loop in phase space is closed.

5.3.3 Assessing the gate performance

With the gate parameters calibrated, we are now able to assess the performance of the entangling operation. There are multiple ways to characterise the gate, such as gate set tomography [40], process tomography [41] or randomised benchmarking [42]. However, these methods typically require addressed single-qubit operations, which are currently not implemented in our setup. Thus, we use a less rigorous approach of applying the gate operation onto one input state and assume that the result would be the same for different input states. For the input state $|\downarrow\downarrow\rangle$, the applied gate sequence is expected to create the Bell state Φ^+. Assuming that after the sequence we find the state described by the density matrix ρ, the fidelity with respect to the Bell state Φ^+ is given by

$$F = \langle\Phi^+|\,\rho\,|\Phi^+\rangle = \frac{1}{2}\left(\rho_{\uparrow\uparrow,\uparrow\uparrow} + \rho_{\downarrow\downarrow,\downarrow\downarrow}\right) + \frac{1}{2}\left(e^{i\Phi}\rho_{\uparrow\uparrow,\downarrow\downarrow} + e^{-i\Phi}\rho_{\downarrow\downarrow,\uparrow\uparrow}\right), \tag{5.3}$$

where $\rho_{ij,kl}$ denotes the matrix element to the corresponding state $|ij\rangle\langle kl|$ for $i,j,k,l = \uparrow,\downarrow$. The first term describes the populations in the states $|\downarrow\downarrow\rangle$ and $|\uparrow\uparrow\rangle$. The second term describes the coherences. Determining the fidelity then reduces to measuring the population given by the first term, and the coherences given by the second term. We can determine the coherences by applying an analysis pulse as shown in figure 5.9(a). It consists of an additional $\pi/2$-pulse that is applied to the Bell state with a variable phase ϕ. This results oscillations of the parity P depending on ϕ, described by [25]

$$P(\phi) = p_{\uparrow\uparrow} + p_{\downarrow\downarrow} - p_{\uparrow\downarrow} - p_{\downarrow\uparrow} \propto A\sin(2\phi + \Phi), \tag{5.4}$$

where the amplitude A corresponds to the coherences term in equation 5.3. From this we find the fidelity by averaging the population and the parity amplitude $F = (p_{\uparrow\uparrow} + p_{\downarrow\downarrow} + A)/2$. Note that we neglect Φ as we are mainly concerned about the degree of entanglement instead of the exact phase of the Bell state.

We determine the fidelity for the 45 µs gate shown in figure 5.9(b) by measuring the populations and the parity. By measuring the population over 2100 repetitions, we find $p_{\uparrow\uparrow} + p_{\downarrow\downarrow} = 0.98(2)$. The parity scan is shown in figure 5.10. The parity is determined via equation 5.4. From the fit parameters, we find $A = 0.92(2)$ and $\Phi = 0.57(1)\pi$. Therefore we find the total fidelity of creating the entangled state $F = 0.95(3)$.

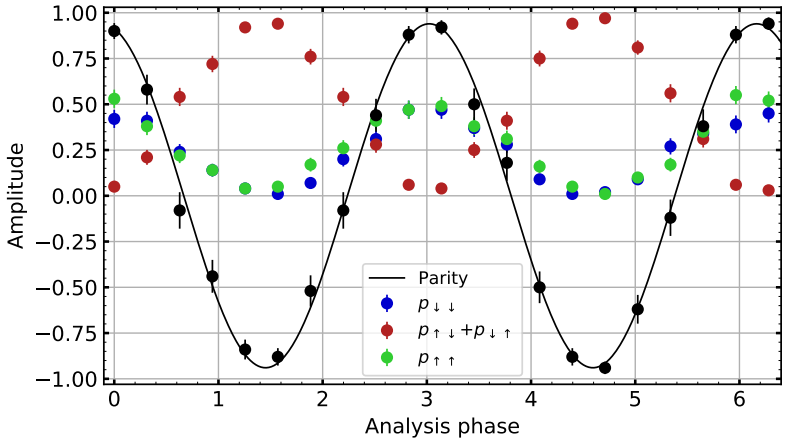

Figure 5.10: Parity scan of a Bell state. The solid line shows a fit from equation 5.4 and yields the amplitude $A = 0.92(2)$ and $\Phi = 0.57(1)\pi$.

5.3.4 Gate implementation within a spin-echo sequence

Another method to create entanglement with the geometric phase gate is to split the gate pulse into two halves and apply an echo pulse after the first gate pulse. This allows for a more robust gate as the effects of unequal $\Omega_\uparrow$ and $\Omega_\downarrow$, as well as single-qubit light-shifts, will be cancelled with the echo pulse.

We set up the two loop gate similarly to the one loop gate discussed in section 5.3.2. Though we lower the power in the $R_\parallel$ beam such that the populations $p_{\downarrow\downarrow} = p_{\uparrow\uparrow}$ are equalised where the second motional loops closes at $2t_g$. The gate is then split into two equal halves and a π-pulse is inserted after the first gate pulse. We scan t to find the point where $p_{\uparrow\downarrow}+p_{\downarrow\uparrow}$ is minimised, then optimise the power in the $R_\parallel$ beam to equalise $p_{\downarrow\downarrow}$ and $p_{\uparrow\uparrow}$. The gate embedded in a spin-echo sequence is shown in figure 5.11. Here, it can be seen that the gate evolution looks almost identical to the gate without the echo pulse. The dip of $p_{\downarrow\uparrow}+p_{\uparrow\downarrow}$ around the 100 µs mark indicate that at this point the two loops in phase space are closed. However, at this point the beam power is too high, leading to an imbalanced population between $p_{\downarrow\downarrow}$ and $p_{\uparrow\uparrow}$. This generally lowers the contrast of the parity oscillation but does not affect the infidelity of the populations.

After setting up one gate, we characterise the gate performance by applying multiple gates within the spin-echo sequence as shown in figure 5.12. Applying multiple gates and monitoring the resulting fidelity after a certain number of gates offers a way to quantify the error per gate more precisely. The reason is that SPAM errors in our experiment are on the same order of magnitude as the gate infidelity, thus limiting the fidelity we are able to observe when performing single gates. When applying multiple gates, the two-qubit gate error accumulates and leads to a decay in Bell state fidelity depending on the number of applied gates.

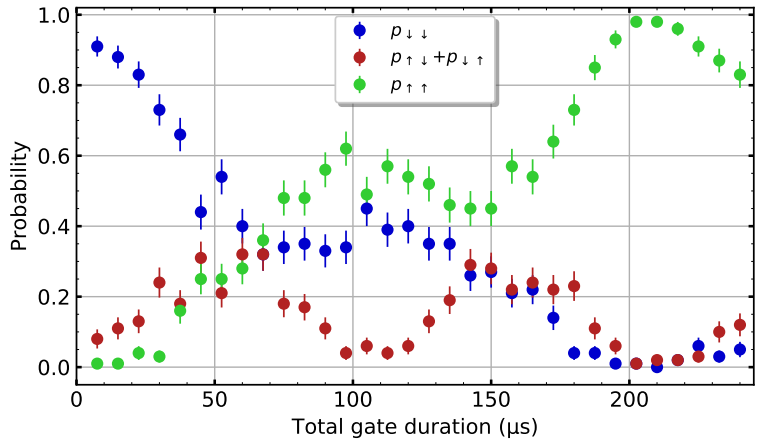

Figure 5.11: Population evolution for a phase gate embedded in a spin-echo sequence. The minimum of $p_{\downarrow\uparrow} + p_{\uparrow\downarrow}$ at $t \approx 100\,\mu s$ indicates that the two loops in phase space are closed.

Since the number of single-qubit operations is constant, they only lead to an offset in the decay curve. It should be noted, when determining the fidelity from the decay curve the extracted fidelity only represents the quality of the light-shift gate, whereas from applying a single gate we extracted the fidelity of the entangling operation which also includes the single-qubit operations.

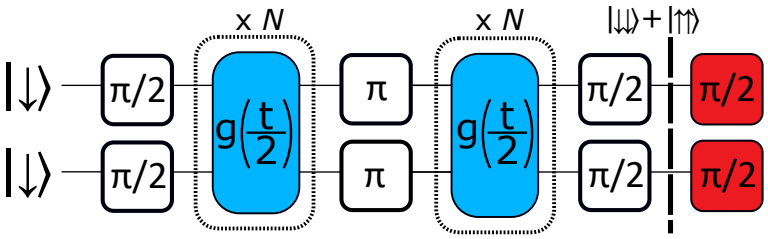

Figure 5.12: Pulse sequence for an entangling gate using the phase gate. The gate pulse $g(t)$ is split into two equal parts and embedded in the arms of a spin-echo sequence. When doing multiple gates to amplify the gate error, $g(t/2)$ is repeated N times in each arm. After the second $\pi/2$ pulse a Bell state $\Phi^{\pm}$ is created. By applying an additional $\pi/2$-pulse with varying phase we obtain parity oscillations.

With the single gate calibrated we now apply N gates in each arm of the spin-echo sequence. We are only interested in the performance when applying an odd number of gates, as a sequence of ideal even number of gates disentangles the qubits. The parity oscillations after 1 and 7 gates for a 125 µs gate are shown in figure 5.13. By fitting equation 5.4 we find the contrasts $A_1 = 0.97(1)$ and $A_7 = 0.87(3)$ and phases $\Phi_1 = 5.38(2)\,\text{rad}$ and $\Phi_7 = 2.44(4)\,\text{rad}$ for 1 and 7 gates,

respectively. In the ideal case, we would expect a π phase difference, since the phase of the Bell state is flipped after every two gates. The deviation from the expected value might be a consequence of the gate's imperfection.

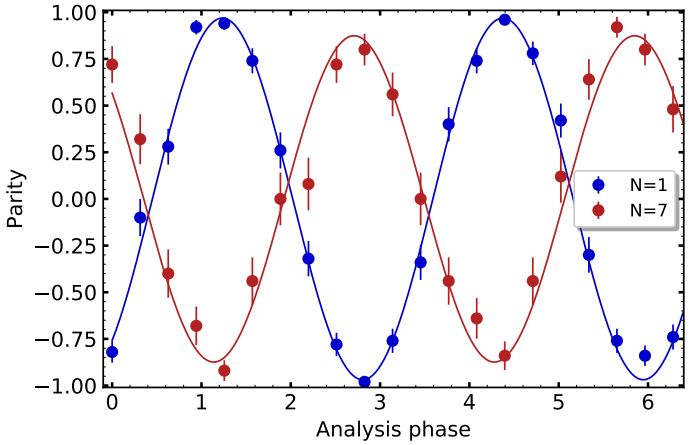

Figure 5.13: Parity scan of the Bell state generated by a single and multiple applications of a 125 µs gate. The solid lines show fits to equation 5.4 to determine the amplitude of the parity oscillation.

We now quantify the error per gate by observing the decay of multiple applied gates. As the gate fidelity is found by averaging the amplitude of the parity oscillation and the population fidelity, we record these for each number of gates. In figure 5.14 we show the decay curves for a 125 µs and a 205 µs gate. For the population fidelity decay curve we notice two outliers that deviate significantly from the expected behaviour at 3 gates of the 125 µs and at 7 gates of the 205 µs gate. It should be noted that due to the drift of the Rabi frequency discussed in section 5.2.3 we usually recalibrate the gate between datapoints. Thus, we suspect that the outliers are caused by imperfect re-calibration.

We estimate the single gate fidelity by extrapolating the decay curves. Due to decoherence, we expect the parity to converge to 0 if the total sequence time is much longer than the coherence time. Similarly, we expect the population fidelity to converge to 0.5, as the populations will be uniformly distributed across the four states due to decoherence. We fit our data to the functions

$$F_{\text{parity}}(N) = \epsilon_{\text{SPAM}} F^N \quad \text{and} \tag{5.5}$$

$$F_{\text{populations}}(N) = \epsilon_{\text{SPAM}}(F^N + 0.5), \tag{5.6}$$

for the parity and the populations decay curve, respectively. Here, ϵ_{SPAM} accounts for the errors in state preparation and readout as well as the local qubit operations. We find the values $F_{125} = 0.994(1)$ and $F_{205} = 0.992(1)$ for the short and long gate respectively.

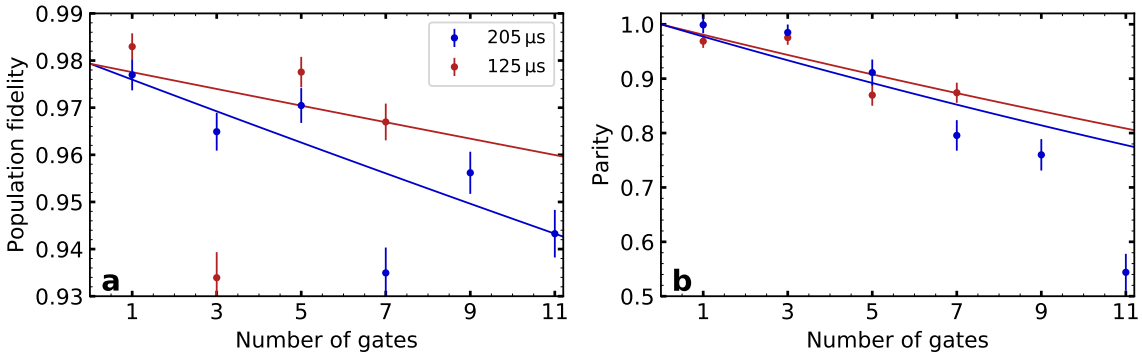

Figure 5.14: Gate decay curve for multiple applied light-shift gates. In (a) the decay of population fidelity is shown, (b) shows the decay of total fidelity. Blue and red data show the decay for a 125 µs and 205 µs gates respectively. The solid lines show exponential decay fits (eq. 5.6) to extrapolate the fidelity of a single gate.

We now compare the measured gate fidelity with a theoretical expectation. We analyse our gate infidelity by using analytical error models described in reference [25]. As the analytical model does not cover spin-decoherence as a function of the decoherence time, we determine the error due to spin-decoherence by simulating equation 3.31 using the Python library QuTiP [43]. The spin-decoherence is simulated by using the collapse operator $\Gamma(\sigma_z \otimes \sigma_z)$ with $\Gamma = 1\sqrt{2\tau_{\mathrm{c,echo}}}$.

Since our infidelity is on the order of 1 %, we only discuss the dominant errors with contributions $> 0.01\,\%$. These include spin-decoherence, motional dephasing, motional heating and off-resonant carrier coupling. The effects of motional heating and dephasing are estimated by using the heating rate $\dot{\bar{n}} = 13\,\mathrm{s}^{-1}$ and motional coherence time $\tau_{\mathrm{motion}} = 80\,\mathrm{ms}$ that were previously measured on this apparatus. The results are shown in table 1. It can be seen that spin-decoherence is the leading source of error. However, the expected infidelity due to spin-decoherence is significantly larger than the measured error. This might possibly be explained by the method used for simulating the error, as using the $\sigma_z \otimes \sigma_z$ collapse operator assumes an exponential decay of the coherence. Though as we have shown in section 5.2.2, the observed decay follows a Gaussian curve. Since initial the gradient of the exponential decay curve is steeper than the gradient of the Gaussian curve, this could overestimate the infidelity. Determining the spin-decoherence error more precisely would require more thorough simulations that are beyond the scope of this thesis.

Error source	$t_g = 125\,\mu s$	$t_g = 205\,\mu s$
Spin-decoherence	1.66 %	2.44 %
Motional dephasing	0.11 %	0.18 %
Motional heating	0.04 %	0.07 %
Off-resonant carrier coupling	0.01 %	0.005 %
Total error	1.82 %	2.70 %
Measured infidelity	0.6(1) %	0.8(1) %

Table 1: Infidelity estimates for the 125 µs and 205 µs light-shift gates. Spin-decoherence is determined by numerical simulations of equation 3.31 with coherence time $\tau_{\text{echo}} = 9.7\,\text{ms}$. Contributions from motional dephasing, motional heating and off-resonant carrier coupling are determined via analytical models from ref. [44].

5.4 Raman Mølmer-Sørensen gate

5.4.1 Setting up the gate

When switching from the light-shift gate to the Raman MS gate, we first need to make physical changes to our setup. The polarisation of the $R_\perp$ beam is rotated by 90° from $\sigma^\pm$ to π via a $\lambda/2$-waveplate. In this configuration, we are able to perform local operations and entangling gate operations with the $R_\perp$ and $R_\parallel$ beams, hence we do not use the R_π beam. Performing single-qubit operations is done with the monochromat configuration of the $R_\parallel$ beam. The frequency $f_{R_\parallel}$ of the monochromat is set such that the frequency difference between the $R_\parallel$ and $R_\perp$ beam matches the carrier transition frequency of the ground state. With this set, we are able to drive coherent Rabi oscillations of the two ions. These will be used to perform the analysis pulse that induces parity oscillations as discussed in section 5.3.3.

After setting up the frequency and power for the single-qubit operation, we set up the gate as follows:

1. We set the rf frequencies and powers of the two components of the bichromatic configuration that are fed to the $R_\parallel$ beam's AOM. For obtaining the Raman $(\sigma_x \otimes \sigma_x)$-interaction, the frequencies of red and blue components of the bichromat have to be chosen symmetric around the carrier transition. First, we choose a desired gate time t_g. The rf frequency of the blue component is then chosen as $f_{R_\parallel} + \omega_z + 2\pi/t_g$ and the red component as $f_{R_\parallel} - \omega_z - 2\pi/t_g$. This will create the gate interaction on the axial COM mode.

2. Next, we equalise the beam powers such that the red and blue component have equal optical powers. The rf power of the two components is calibrated

by feeding them to the $R_{\parallel}$ beam's AOM and monitoring the optical power that reaches the trap on a photodiode. We first turn off the blue component and set the rf power of the red component to obtain the desired optical power P_o. The red component is then turned off and we turn on the blue component and set its rf power such that the optical power at the photodiode matches P_o.

3. When the frequencies and powers of the beams are set, we further optimise the sequence parameters by optimising the gate interaction on two ions. We do this by preparing the ions in $|\downarrow\downarrow\rangle$ and applying the bichromatic gate pulse. The gate pulse is implemented by simultaneously illuminating the ions with the $R_{\perp}$ beam and the $R_{\parallel}$ beam with the bichromatic configuration. By varying the duration of the gate pulse we find the time at which the second motional loops close. This is expected after $t = 2t_g$ and is indicated when $p_{\downarrow\uparrow} + p_{\uparrow\downarrow}$ is minimised. After this, we choose the power of the $R_{\perp}$ beam such that $p_{\uparrow\uparrow}$ is maximised at $2t_g$.

4. In order to balance out unequal Rabi frequencies of the blue and red component of the bichromat, one can now scan the frequency $R_{\perp}$ beam in the range of a few 1 kHz to maximise $p_{\uparrow\uparrow}$ even further.

We usually repeat this process to find the optimal parameters. After the optimisation, we expect to observe an entangled state when applying the gate pulse for t_g, indicated by $p_{\uparrow\uparrow} = p_{\downarrow\downarrow} = 0.5$.

5.4.2 Results

The results for a 59 µs MS gate are shown in figure 5.15. The evolution of the population is similar to the light-shift gate presented in section 3.3.1. We observe that the motional loops are closed at $t = 59$ µs and $t = 120$ µs, as indicated by the minima of $p_{\downarrow\uparrow} + p_{\uparrow\downarrow}$. Equal populations in $p_{\downarrow\downarrow}$ and $p_{\uparrow\uparrow}$ indicate the generation of an entangled state. This entangled state is again disentangled after the second loop.

As explained in section 5.3.3 we induce parity oscillations by an analysis pulse to determine the fidelity of the gate. The results are shown in figure 5.15. From a fit to equation 5.4 we find the amplitude $A = 0.999(6)$ and phase $\Phi = 3.14(4)$. Together with the population fidelity $p_{\downarrow\downarrow}+p_{\uparrow\uparrow} = 0.986(4)$ we find the overall fidelity $F = 0.993(3)$.

As done in section 5.3.4, we now apply multiple gates to monitor the gate decay and extrapolate the fidelity of a single gate. The population and fidelity decay for a different number of gates are shown in figure 5.16. We extrapolate the single-gate population fidelity and parity by fitting our data to equation 5.6. We find $F = 0.996(1)$.

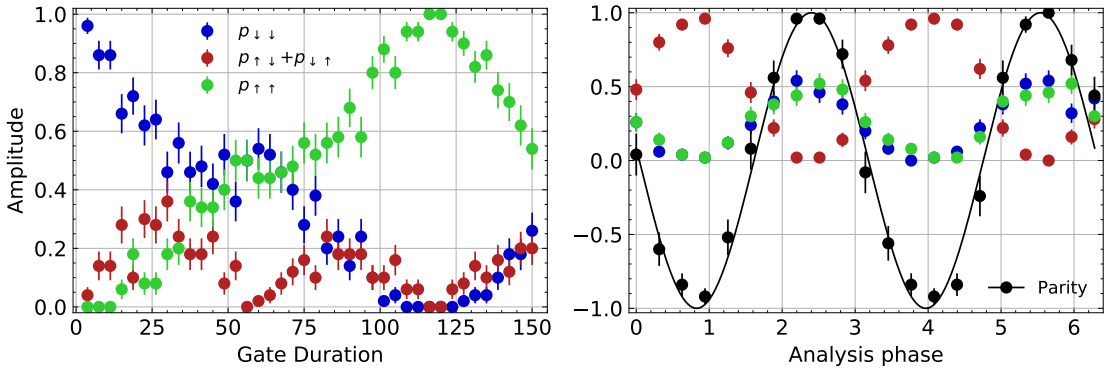

Figure 5.15: Population dynamics of the Raman MS gate. Left: Population dynamics for different lengths of the gate pulse. At $t = 59\,\mu s$ the loops in phase space are closed and the ions are in the entangled state $|\uparrow\uparrow\rangle + |\downarrow\downarrow\rangle$. Applying the gate pulse for longer times disentangles the state until the ions are completely transferred to the state $|\uparrow\uparrow\rangle$ at $t = 120\,\mu s$. Right: Scanning the phase of a $\pi/2$-pulse applied to the Bell state created at $t = 59\,\mu s$ leads to parity oscillations. The solid line represents a fit to equation 5.4 with amplitude $A = 99.9(6)$ and phase $\Phi = 3.14(4)$.

We estimate the expected gate error as done in section 5.3.4. The total expected error is 0.81 %. As in section 5.3.4, the largest contribution is caused by spin-decoherence with an estimated error of 0.72 %. This is again significantly larger than the measured infidelity $1 - F = 0.4(1)\,\%$ and might be explained by the fact that the simulation assumes an exponential decay, as discussed in section 5.3.4.

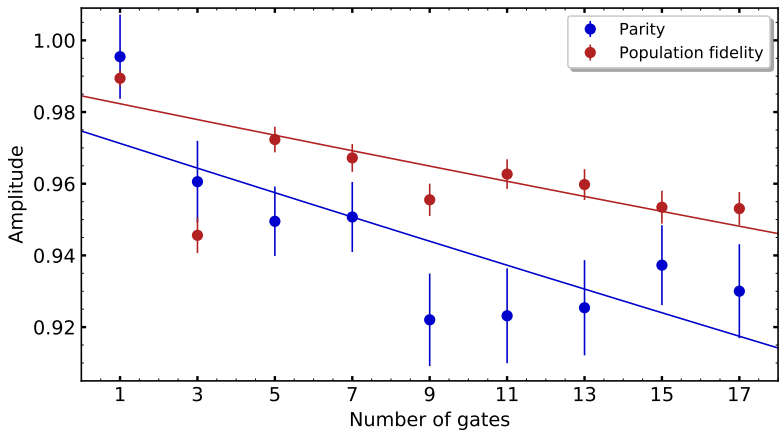

Figure 5.16: Gate decay curve for multiple applied Raman MS gates. Solid lines are fits of equation 5.6 to the Bell state and population fidelity. By averaging the extrapolated population fidelity and parity we find the total fidelity $F = 0.996(1)$.

6 Conclusion and Outlook

In the course of this thesis we have created a setup to implement coherent Raman interactions on the ground state of $^{40}Ca^{+}$ ions. These interactions were used to implement quantum logic gates on the ground state qubit of $^{40}Ca^{+}$. We have demonstrated local qubit operations on a single ion and two ions. Moreover, we have presented two methods to entangle two ions in their ground state.

We used the setup for local qubit operations on $^{40}Ca^{+}$ ions. First, we have performed spectroscopy on the ground state carrier transition and the blue sidebands of the axial motional modes. With Rabi oscillations, we have shown that we can coherently transfer the state populations between the two ground states. By employing Ramsey and spin-echo sequences we were able to determine the coherence time of our system. Next, we investigated the effect of beam alignment on the quality of Rabi oscillations. We found that centring the beam on the ion enhances the Rabi decay time constant. Finally, we have shown Rabi oscillations of two ions with a relative Rabi frequency difference of less than 1 %.

We entangled two $^{40}Ca^{+}$ ions by using the light-shift gate embedded in Ramsey and spin-echo sequences. For a single gate embedded in a Ramsey sequence we observed a Bell state fidelity of 95(3) %. By performing a two-loop light-shift gate within a spin-echo sequence we were able to increase the single gate fidelity above 99 %. As this is on the same order of magnitude as our SPAM errors, we applied multiple subsequent gates to amplify the gate error without increasing the SPAM error. From the gate decay curve we extrapolated a single gate fidelity of 99.4(1) % for a 125 µs gate.

Finally, we created a Mølmer-Sørensen type interaction by modulating one Raman beam with a bichromatic electromagnetic field. With this we were able to entangle two ions in their ground state. We applied multiple subsequent gates to obtain a gate decay curve. From this we determined a single gate fidelity of 99.6(1) %.

The currently largest contribution limiting our setup's performance is spin-decoherence. We suspect that this is mainly caused by phase instabilities between beam paths of the orthogonal beam pair. We suspect that we could reduce this effect by reducing the mechanical vibrations of the optical setup or by reducing the length of the beam paths by re-arranging the optical setup at the trap in a more compact way. A different approach would be to implement active phase stabilisation via a feedback loop.

For future experiments, we are currently working on implementing single-qubit and two-qubit operations for a qubit encoded in the ground state of $^{88}Sr^{+}$ ions. As a next step, we want to use the light-shift gate to create entanglement of a mixed-species $^{88}Sr^{+}$-$^{40}Ca^{+}$ ion crystal. The setup presented in this thesis could also be used to implement the $\sigma_z \otimes \sigma_z$ light-shift gate on the optical qubit as suggested in

ref. [45]. Both methods would expand the current toolbox of our experiment and enable experiments for mixed-species quantum logic experiments.

References

[1] D. Deutsch and R. Jozsa, "Rapid Solution of Problems by Quantum Computation," *Proceedings of the Royal Society of London Series A*, 439, 553–558, 1992.

[2] P. Shor, "Algorithms for quantum computation: Discrete logarithms and factoring," in *Proceedings 35th Annual Symposium on Foundations of Computer Science*, Santa Fe, NM, USA: IEEE Comput. Soc. Press, 1994, pp. 124–134.

[3] L. K. Grover, "Quantum Mechanics Helps in Searching for a Needle in a Haystack," *Physical Review Letters*, 79, 325–328, 1997.

[4] D. P. DiVincenzo, "The Physical Implementation of Quantum Computation," *Fortschritte der Physik*, 48, 771–783, 2000.

[5] M. H. Devoret and R. J. Schoelkopf, "Superconducting Circuits for Quantum Information: An Outlook," *Science*, 339, 1169–1174, 2013.

[6] S. Slussarenko and G. J. Pryde, "Photonic quantum information processing: A concise review," *Applied Physics Reviews*, 6, 041303, 2019.

[7] M. Saffman, T. G. Walker, and K. Mølmer, "Quantum information with Rydberg atoms," *Reviews of Modern Physics*, 82, 2313–2363, 2010.

[8] J. Preskill, "Quantum Computing in the NISQ era and beyond," *Quantum*, 2, 79, 2018.

[9] F. Arute *et al.*, "Quantum supremacy using a programmable superconducting processor," *Nature*, 574, 505–510, 2019.

[10] D. Kielpinski, C. Monroe, and D. J. Wineland, "Architecture for a large-scale ion-trap quantum computer," *Nature*, 417, 709–711, 2002.

[11] M. A. Nielsen and I. L. Chuang, *Quantum Computation and Quantum Information*. Cambridge ; New York: Cambridge University Press, 2000.

[12] C. H. Bennett, F. Bessette, G. Brassard, L. Salvail, and J. Smolin, "Experimental quantum cryptography," *Journal of Cryptology*, 5, 3–28, 1992.

[13] P. Ghosh, *Ion Traps*. Clarendon Press, 1995.

[14] D. Leibfried, R. Blatt, C. Monroe, and D. Wineland, "Quantum dynamics of single trapped ions," *Reviews of Modern Physics*, 75, 281–324, 2003.

[15] D. James, "Quantum dynamics of cold trapped ions with application to quantum computation," *Applied Physics B*, 66, 181–190, 1998.

[16] D. Wineland, C. Monroe, W. Itano, D. Leibfried, B. King, and D. Meekhof, "Experimental issues in coherent quantum-state manipulation of trapped atomic ions," *Journal of Research of the National Institute of Standards and Technology*, 103, 259, 1998.

[17] I. Pogorelov, T. Feldker, C. D. Marciniak, G. Jacob, V. Podlesnic, M. Meth, V. Negnevitsky, M. Stadler, K. Lakhmanskiy, R. Blatt, P. Schindler, and T. Monz, "A compact ion-trap quantum computing demonstrator," *arXiv:2101.11390 [quant-ph]*, 2021.

[18] R. Bowler, J. Gaebler, Y. Lin, T. R. Tan, D. Hanneke, J. D. Jost, J. P. Home, D. Leibfried, and D. J. Wineland, "Coherent Diabatic Ion Transport and Separation in a Multizone Trap Array," *Physical Review Letters*, 109, 080502, 2012.

[19] M. W. van Mourik, E. A. Martinez, L. Gerster, P. Hrmo, T. Monz, P. Schindler, and R. Blatt, "Coherent rotations of qubits within a surface ion-trap quantum computer," *Physical Review A*, 102, 022611, 2020.

[20] T. Ruster, C. Warschburger, H. Kaufmann, C. T. Schmiegelow, A. Walther, M. Hettrich, A. Pfister, V. Kaushal, F. Schmidt-Kaler, and U. G. Poschinger, "Experimental realization of fast ion separation in segmented Paul traps," *Physical Review A*, 90, 033410, 2014.

[21] C. J. Foot, *Atomic physics*, ser. Oxford master series in physics 7. Atomic, Optical, and laser physics. Oxford ; New York: Oxford University Press, 2005.

[22] M. Brownnutt, M. Kumph, P. Rabl, and R. Blatt, "Ion-trap measurements of electric-field noise near surfaces," *Reviews of Modern Physics*, 87, 1419–1482, 2015.

[23] D. F. James and J. Jerke, "Effective Hamiltonian theory and its applications in quantum information," *Canadian Journal of Physics*, 85, 625–632, 2007.

[24] V. Schafer, "Fast gates and mixed-species entanglement with trapped ions," PhD Thesis, University of Oxford, 2018.

[25] C. Ballance, "High-fidelity quantum logic in Ca^+," PhD Thesis, University of Oxford, 2014.

[26] K. Mølmer and A. Sørensen, "Multiparticle Entanglement of Hot Trapped Ions," *Physical Review Letters*, 82, 1835–1838, 1999.

[27] W. Magnus, "On the exponential solution of differential equations for a linear operator," *Communications on Pure and Applied Mathematics*, 7, 649–673, 1954.

[28] R. J. Glauber, "The Quantum Theory of Optical Coherence," *Physical Review*, 130, 2529–2539, 1963.

[29] A. C. Hughes, V. M. Schäfer, K. Thirumalai, D. P. Nadlinger, S. R. Woodrow, D. M. Lucas, and C. J. Ballance, "Benchmarking a High-Fidelity Mixed-Species Entangling Gate," *Physical Review Letters*, 125, 080504, 2020.

[30] M. Hettrich, T. Ruster, H. Kaufmann, C. F. Roos, C. T. Schmiegelow, F. Schmidt-Kaler, and U. G. Poschinger, "Measurement of Dipole Matrix Elements with a Single Trapped Ion," *Physical Review Letters*, 115, 143003, 2015.

[31] M. Ramm, T. Pruttivarasin, M. Kokish, I. Talukdar, and H. Häffner, "Precision Measurement Method for Branching Fractions of Excited $P_{1/2}$ States Applied to $^{40}Ca^{+}$," *Physical Review Letters*, 111, 023004, 2013.

[32] A. H. Myerson, D. J. Szwer, S. C. Webster, D. T. C. Allcock, M. J. Curtis, G. Imreh, J. A. Sherman, D. N. Stacey, A. M. Steane, and D. M. Lucas, "High-fidelity readout of trapped-ion qubits," *Phys. Rev. Lett.*, 100, 200502, 2008.

[33] P. A. Barton, C. J. S. Donald, D. M. Lucas, D. A. Stevens, A. M. Steane, and D. N. Stacey, "Measurement of the lifetime of the $3d^2D_{5/2}$ state in $^{40}Ca^{+}$," *Physical Review A*, 62, 032503, 2000.

[34] A. Bermudez, X. Xu, R. Nigmatullin, J. O'Gorman, V. Negnevitsky, P. Schindler, T. Monz, U. G. Poschinger, C. Hempel, J. Home, F. Schmidt-Kaler, M. Biercuk, R. Blatt, S. Benjamin, and M. Müller, "Assessing the Progress of Trapped-Ion Processors Towards Fault-Tolerant Quantum Computation," *Physical Review X*, 7, 041061, 2017.

[35] A. Erhard, J. J. Wallman, L. Postler, M. Meth, R. Stricker, E. A. Martinez, P. Schindler, T. Monz, J. Emerson, and R. Blatt, "Characterizing large-scale quantum computers via cycle benchmarking," *Nature Communications*, 10, 5347, 2019.

[36] M. Chwalla, "Precision spectroscopy with $^{40}Ca^{+}$ ions in a Paul trap," Ph.D. dissertation, University of Innsbruck, 2009.

[37] H. Kaufmann, "A Scalable Quantum Processor," Ph.D. dissertation, Universität Mainz, 2017.

[38] M. Brandl, "Towards Cryogenic Scalable Quantum Computing with Trapped Ions," Ph.D. dissertation, University of Innsbruck, 2016.

[39] P. Schindler, "Frequency synthesis and pulse shaping for quantum information processing with trapped ions," Diploma thesis, University of Innsbruck, 2008.

[40] E. Nielsen, J. K. Gamble, K. Rudinger, T. Scholten, K. Young, and R. Blume-Kohout, "Gate Set Tomography," *arXiv:2009.07301 [quant-ph]*, 2020.

[41] I. L. Chuang and M. A. Nielsen, "Prescription for experimental determination of the dynamics of a quantum black box," *Journal of Modern Optics*, 44, 2455–2467, 1997.

[42] E. Knill, D. Leibfried, R. Reichle, J. Britton, R. B. Blakestad, J. D. Jost, C. Langer, R. Ozeri, S. Seidelin, and D. J. Wineland, "Randomized benchmarking of quantum gates," *Physical Review A*, 77, 012307, 2008.

[43] J. R. Johansson, P. D. Nation, and F. Nori, "QuTiP 2: A Python framework for the dynamics of open quantum systems," *Computer Physics Communications*, 184, 1234–1240, 2013.

[44] C. J. Ballance, V. M. Schäfer, J. P. Home, D. J. Szwer, S. C. Webster, D. T. C. Allcock, N. M. Linke, T. P. Harty, D. P. L. Aude Craik, D. N. Stacey, A. M. Steane, and D. M. Lucas, "Hybrid quantum logic and a test of Bell's inequality using two different atomic isotopes," *Nature*, 528, 384–386, 2015.

[45] B. C. Sawyer and K. R. Brown, "Wavelength-insensitive, multispecies entangling gate for group-2 atomic ions," *Phys. Rev. A*, 103, 022427, 2021.

Acknowledgements

With this thesis coming to an end I would like to thank the people without whom this work would not have been possible. First, I would like to thank Rainer Blatt for allowing me to carry out my thesis in his group and being part of such a wonderful team of researchers.

I would like to thank the senior members of the quantum information team. Thomas Monz for his guidance throughout the course of my work and critical comments on my thesis. Big thanks to Philipp Schindler for inviting me to this experiment and offering me to work on such an interesting project, for the support during my stay in this group and for the thorough corrections to my thesis.

Special thanks go out to my labmates Lukas Gerster, Martin van Mourik and Pavel Hrmo for their support since the first day in the lab. Thank you for helping me in building this setup and carrying out this work, for teaching me about trapped ions and always tirelessly answering my questions.

I would like to thank all the members of the Blatt and Northup group for the welcoming and helpful atmosphere.

Zum Schluss möchte ich mich bei meiner Familie und bei meiner Freundin Melanie für all die Unterstützung der vergangenen Jahre bedanken. Diese Arbeit wäre ohne euch nicht möglich gewesen. Auch danke ich all meinen Freunden für die unvergessliche Zeit der letzten Jahre.